

# 1            **BOUNDING THE UNCERTAINTY OF FLUX DIVERGENCE CALCULATIONS IN** 2            **RADAGAST**

3 J. J. Settle (communicating author)  
4 N. A. Bharmal  
5 G. J. Robinson  
6 A. Slingo

7 Environmental Systems Science Centre  
8 The University of Reading  
9 Whiteknights  
10 Reading  
11 RG6 6AL  
12 UK

14 [jjj@mail.nerc-essc.ac.uk](mailto:jjj@mail.nerc-essc.ac.uk)

## 15            **ABSTRACT**

16 In the RADAGAST project we calculate the divergence of radiative flux across the  
17 atmosphere by comparing fluxes measured at each end of an atmospheric column above  
18 Niamey, in the African Sahel region. The combination of broad band flux measurements  
19 from geostationary orbit, and the deployment for over twelve months of a comprehensive  
20 suite of active and passive instrumentation at the surface, eliminates a number of sampling  
21 issues that could otherwise affect divergence calculations of this sort. However, one sampling  
22 issue that challenges the project is the fact that the surface flux data are essentially  
23 measurements made at a point, while the top-of-atmosphere values are taken over a solid  
24 angle that corresponds to an area at the surface of some 2500 square kilometres. Variability  
25 of cloud cover and aerosol loading in the atmosphere mean that the downwelling fluxes, even  
26 when averaged over a day, will not be an exact match to the area-averaged value over that  
27 larger area, although we might expect that it is an unbiased estimate thereof. The  
28 heterogeneity of the surface, for example fixed variations in albedo, further means that there  
29 is a likely systematic difference in the corresponding upwelling fluxes.

30 In this paper we characterise and quantify this spatial sampling problem. We bound the root-  
31 mean-square error in the downwelling fluxes by exploiting a second set of flux measurements  
32 from a site that was run in parallel with the main deployment. The flux differences lead us to  
33 an upper bound to the sampling uncertainty, and their correlation leads to another which is  
34 probably optimistic as it requires certain other conditions to be met. For the upwelling fluxes  
35 we use data products from a number of satellite instruments to characterise the relevant  
36 heterogeneities and so estimate the systematic effects that arise from the flux measurements  
37 having to be taken at a single point. We find that the sampling errors for the daily average  
38 flux are small for the irradiance under relatively clear skies, generally less than  $5\text{Wm}^{-2}$ , but  
39 these increase to about  $10\text{Wm}^{-2}$  during the African monsoon season. For the upwelling  
40 fluxes, again taking daily averages, systematic errors are of order  $10\text{Wm}^{-2}$  as a result of  
41 albedo differences, but rather less than this for the longwave component of the surface  
42 radiation budget.

---

## 1 INTRODUCTION

43  
44  
45  
46  
47  
48  
49  
50  
51  
52  
53  
54  
55  
56  
57  
58  
59  
60  
61  
62  
63  
64  
65  
66  
67  
68  
  
69  
70  
71  
72  
73

Of the solar radiation that arrives at the top of the atmosphere, some 30% is reflected directly back to space, approximately half is absorbed at the surface, and the remainder is absorbed by the atmosphere. These are global averages, and there is some uncertainty over the totals. Kiehl and Trenberth (1997), in perhaps the most widely quoted figure, calculated the amount absorbed by the atmosphere as  $67\text{Wm}^{-2}$ . However, other estimates range as high as  $93\text{Wm}^{-2}$  (Wild et al., 1995). Unfortunately, we cannot directly observe the divergence of radiative flux across the atmosphere, and it has to be calculated as a residual: we must estimate flux budgets at the top and bottom of an atmospheric column and take their difference. The flux budget at the top of the atmosphere can only be obtained using measurements taken from space, and as most Radiation Budget instruments have until recently been located on low earth orbit satellites, it has been difficult to achieve adequate sampling of the diurnal cycles of the fluxes. The satellite-based measurements also define the horizontal scale of the column we must deal with. This is typically tens of kilometres. It is not feasible to measure the surface radiation budget accurately at more than a few places within such a large footprint, and an uncertainty therefore exists in the final divergence because of the consequent spatial sampling problem. Heterogeneity in the atmosphere, principally sub-footprint variations in cloud cover, means that the downwelling fluxes retrieved from a single surface site will not be the same as the required area average, although we might hope that if we average for long enough, the mean atmospheric conditions seen at a point will be close to those averaged over the required area. Over the land surface a second difficulty arises from the variability of the radiative properties of the surface over relatively short scales. This means that reflected shortwave flux, and emitted longwave flux, are likely to be systematically different from the required area averages of those quantities. Thus, if we use the point fluxes in our calculations, without any attempt to blend these with other data in some way to estimate the appropriate area averages, we can expect to suffer from a degree of sampling error.

In this paper we characterise these uncertainties for the particular case of the RADAGAST study, although to understand them completely we would need to know far more about the large-area surface radiation budget than we can measure. Satellite-derived data sets of surface properties are used to characterise the surface heterogeneities that are the cause of the uncertainty in the upwelling fluxes, and we infer details of the spatial variability of

---

74 downwelling fluxes from combining two sets of flux measurements separated by an  
75 appropriate distance.

## 76 **1.1 RADAGAST**

77 The RADAGAST project (Miller and Slingo, 2007, hereafter M&S) was set up with the  
78 intention of enabling more accurate calculations of atmospheric divergence (and heating rates,  
79 etc.). The project ran during the last months of 2005, and for the whole of 2006, and was  
80 closely associated with the regional AMMA (African Monsoon Multi-disciplinary Analyses)  
81 project, an extensive collaboration between European, African and American scientists to  
82 study aspects of the West African Monsoon (Redelsperger et al., 2006). The idea of  
83 RADAGAST was to take advantage of two recent developments that would, together, enable  
84 us to tie down better the bounding radiation budgets that define the atmospheric divergence  
85 without being compromised by poor diurnal sampling of the fluxes. One of these  
86 developments was the deployment of a radiation budget instrument in geostationary orbit, so  
87 that the diurnal flux cycle could be captured. This, the Geostationary Earth Radiation Budget  
88 instrument (Harries et al, 2005), is a broadband radiation sensor that acquires shortwave  
89 (directional) flux and total flux; by subtraction the longwave flux component is obtained.  
90 These are acquired every 5 minutes for the whole of that part of the globe visible to the  
91 instrument, and so can capture the diurnal variability of the top-of-atmosphere fluxes. The  
92 instrument is aboard satellites of the Meteosat Second Generation series, in geostationary  
93 orbit close to the zero meridian, so the instrument obtains fluxes over the Southern Atlantic  
94 ocean, the whole of Africa, Europe and the Middle East; it has a footprint of some 50km at  
95 the sub-satellite point. The platform carries, in addition, a multispectral imager called  
96 SEVIRI (Schmetz et al, 2002) which measures narrow band radiance in 11 channels and has a  
97 footprint of 3km at the sub-satellite point. The SEVIRI data are used for accurate geo-  
98 location of the GERB data, for scene identification (needed for radiance to flux conversion)  
99 and are also used to generate a high-resolution flux product at 9km resolution (Dewitte et al,  
100 2008).

101 A number of fixed stations exist around the world that measure, more or less continuously,  
102 surface radiative fluxes, both upward and downward, longwave and shortwave. The World  
103 Climate Research Program oversees the operation of the Baseline Surface Radiation Network  
104 (BSRN) which deploys 30-40 flux stations around the world, but mostly in Europe and North  
105 America. An important contribution to this capability is provided by the US Atmospheric

---

106 Radiation Measurement (ARM) program, which in addition to taking the standard broadband  
107 flux measurements also maintains at each of its sites a variety of additional instruments for  
108 the study of clouds and aerosols. Unfortunately, none of the fixed ARM stations can be seen  
109 by GERB, and the second development that makes RADAGAST possible is the recent  
110 creation by ARM of a mobile facility, comprising an extensive suite of active and passive  
111 instruments in addition to the broad-band flux instrument (M&S). This, the ARM Mobile  
112 Facility (AMF) was deployed at the main airport at Niamey, republic of Niger (lat:13.482 N,  
113 long: 2.184E) from late 2005, and measurements continued into early 2007. The main  
114 reasons for the selection of Niamey are the wide range of atmospheric conditions experienced  
115 there in any single year, and the excellent logistic support (M&S).

116 In addition to the main deployment, a second set of surface flux data was located at  
117 Banizoumbou (lat: 13.541N, long: 2.665E), located some 53km to the east of Niamey. In the  
118 rest of this document, the label NIA will be used to denote measurements at the main site, and  
119 BAN to label those from the auxiliary site. The relative locations of the two sites are shown  
120 in Figure 1. The background is a MODIS temperature map of the area. The two large  
121 squares delineate the GERB pixels that contain each of the sites; the small square containing  
122 the cross marking Niamey airport is the corresponding resolution-enhanced cell.

## 123 **1.2 Spatial Sampling**

124 Bringing these two elements, GERB and the AMF, together in the RADAGAST project  
125 makes possible the first well (temporally-)sampled broad-band flux measurements  
126 simultaneously at the top and bottom of the atmosphere, with sufficient frequency to capture  
127 the diurnal cycle in radiative flux, so eliminating many of the uncertainties previously  
128 associated with flux divergence calculations. The principal sampling effect that remains for  
129 us to consider is that of the mismatch in spatial scale between the measurements made at the  
130 surface, and those made at the top of the atmosphere. The latter correspond to a surface  
131 footprint of some 50kmX50km, whereas the surface instruments can see only a small part of  
132 the surface flux field that contributes to the fluxes seen by GERB. The downwelling fluxes  
133 also are rather limited in their support, but it is expected that the continuous measurements  
134 mean that, over a suitable period of time, the time-averaged downwelling flux at the sensor is  
135 a good surrogate for the time-averaged flux averaged spatially over the GERB footprint.  
136 However, it is difficult to quantify this assertion, and little work seems to have been done on the  
137 uncertainty to be expected in the point-area comparison. We begin to address some of these

---

138 issues by exploiting the fact that there were two sets of ARM flux instruments. The two sites  
139 are separated by a distance similar to that between the centres of two adjacent GERB pixels,  
140 so the correspondence in the two sets of irradiance measurements permits us to come to some  
141 judgement on how well either represents the required spatial average of the same quantity.

### 142 **1.3 Data processing**

143 Upwelling and downwelling surface fluxes, both longwave and shortwave, are generated  
144 every minute at the AMF stations. The mean flux was calculated for each day at each site,  
145 and these daily values are the principal data sets used here. The average was taken from  
146 midnight to midnight for the longwave instruments, and from sunrise to sunset for the  
147 shortwave. For most days, there is a complete set of data at both sites.

148 The processing chain for the GERB instrument makes use of the higher-resolution SEVIRI  
149 imager, and this also allows the generation of two main products: one of these corrects for the  
150 point spread function of the instrument, so that the resulting flux corresponds to flux arising  
151 equally from all points within a defined area, while the other retains the spatial response  
152 function of the GERB instrument. A third, resolution-enhanced product known as SHI, is  
153 created by distributing the observed flux spatially according to the observed spatial radiance  
154 distributions seen by the SEVIRI; this product has a spatial resolution of 9 km, but is not used  
155 in this study.

156 With the satellite products we have usually done more than compute the required averages  
157 and scatter values, and all the hard work has been done in generating the products in the first  
158 place. Some additional processing was needed to generate daily averages from a land surface  
159 temperature product, but this will be described in the appropriate section.

160 In the next section the flux time series at the two sites are compared. In section 3, we  
161 describe and develop the tools that are used to characterise the sampling error for the  
162 downwelling fluxes. These include an estimate of the error variance in the irradiances that  
163 depends on the correlation coefficient between the two sites, and an upper estimate based on  
164 simpler statistics that limits the effects of non-stationarity in the irradiances. In section 4 the  
165 various contributions to the sampling error, both downwelling and upwelling are considered  
166 separately. For the upwelling fluxes these are based on spatial datasets mapping the albedo  
167 and emissivity of the area, and of the space-time variation in surface temperatures. In section  
168 5 we present estimates of the total uncertainty, month by month, for the major part of 2006.

---

169

## 2 MEAN STATISTICS OF THE SURFACE FLUXES

### 170 **2.1 Shortwave fluxes**

171 The average daily shortwave irradiances could be calculated for most days in 2006.  
172 However, the instruments at Banizoumbou were closed down on Dec 8 2006, and in addition  
173 there were a number of days when no, or only limited, SW data were recorded at that site.  
174 These days are ignored in the comparisons presented here. On some other days a few data  
175 points were missed, but not enough to affect significantly the mean daily fluxes observed.  
176 Linear interpolation was used to fill in those short gaps before calculation of the daily  
177 average. The daily fluxes at the main site at Niamey are analysed in depth in Slingo et al  
178 (2008).

179 There were 331 days in 2006 for which both sites had useful measurements for shortwave  
180 fluxes, and the basic statistics of these fluxes are shown in Table 1. The daily shortwave  
181 irradiances are plotted in Figure 2. The general features of the plot are driven by illumination  
182 geometry, responsible for the increase in irradiance in the early part of the year, and cloud  
183 cover, which is responsible for the recurring drops during the dry season, and the very rapid  
184 fluctuations during the monsoon months of July, August and September.

185 We see that in the early part of the year there are occasional dips in the irradiance, which  
186 happen on cloudy days, but that the two irradiance curves are well matched: the daily  
187 averages at 53km separation follow each other closely, which leads us to expect that the daily  
188 average at a point is indeed a good estimate of the daily average over a 50km square area.  
189 The sampling error appears intuitively to be quite small here (and will be quantified later).  
190 The summer, monsoon season sees greater variability in the shortwave flux, but the two sites  
191 are still well matched as far as the daily average goes (Figure 3). However, on several days  
192 differences of over  $30\text{Wm}^{-2}$  are seen, and occasionally these differences are larger than  
193  $50\text{Wm}^{-2}$ .

194 Smoothed versions of the curves of shortwave irradiance are shown in Figure 4, and the  
195 difference of the two smoothed curves in Figure 5. The detailed shape of these curves varies  
196 with a smoothing parameter, and heavier smoothing of the original curves reduces the  
197 oscillations in the difference curve, while keeping the mean difference constant. It is  
198 probably not a good idea to read too much into the shape of the graph, although it is clear that

---

199 the difference is not constant throughout the year, and that the biggest variations are  
200 associated with the later part, and end of, the monsoon period.

201 The daily SW irradiances for the two sites are shown as a scatterplot in Figure 6. The two  
202 lines either side of the 1-1 line are  $10\text{Wm}^{-2}$  different from that line; points lying outside are  
203 those that differ by more than  $10\text{Wm}^{-2}$ , or in other words lie more than  $7\text{Wm}^{-2}$  from the  
204 nearest point on the 1-1 line. There are more of these (69) below the set of lines than above it  
205 (37), consistent with the greater mean shortwave irradiances seen at site BAN, and the  
206 slightly higher level of cloud cover seen at NIA.

## 207 **2.2 Longwave fluxes**

208 There were 323 days in 2006 with complete or nearly-complete longwave flux measurements  
209 at both sites. A small number of days had large gaps in the 60-second data from which the  
210 averages were calculated, and those days were not used in these comparisons. The statistics  
211 for the downwelling longwave fluxes for those 323 days are shown in Table 2.

212 A scatterplot of the daily mean downwelling longwave flux at the two sites (Figure 7) shows  
213 a systematic difference, with the fluxes at the airport being some  $7\text{Wm}^{-2}$  higher, on average,  
214 than those at the auxiliary site. This difference is almost independent of time of year, yet the  
215 daily means of the near-surface temperatures recorded by the met instruments at the two sites  
216 are within a degree of each other for most of the year. A study prepared for the DOE (Dutton  
217 et al 2008) found no plausible explanation for this difference in terms of atmospheric  
218 conditions, but noted anomalous temperature readings for the instrument case and dome  
219 temperatures, which are used in the calibration of the flux. The likelihood is that the  
220 downward fluxes at BAN are systematically too low, and that the real difference in the means  
221 is much smaller than the  $7\text{Wm}^{-2}$  observed.

222 The relationship between the upward and downward fluxes at either site shows a great deal  
223 more scatter, as we would expect, but it is noticeable that the scatterplots for the two sites are  
224 quite similar (Figure 8), suggesting that the same things are going on at both sites. A  
225 comparison of the upward fluxes, which we might expect to be nuanced given the different  
226 thermal environments at the two sites, instead shows high correlation (Figure 9). Again, there  
227 is an offset of about  $7\text{Wm}^{-2}$  between the two. So, despite the apparently complex relationship  
228 between downwelling and emitted fluxes manifest in Figure 8, the uncorrected net fluxes are  
229 found to be very highly correlated (Figure 10).

---

230 The longwave component of the surface radiation budget is typically between 50 and 150  
231  $\text{Wm}^{-2}$  for the daily means. There is a noticeable seasonal variation to this, tied to variations in  
232 atmospheric humidity and cloud cover, as we can see in Figure 11, which shows the daily net  
233 LW fluxes for the two sites. The maximum in the net flux occurs at the end of the dry  
234 season, when the surface temperature is high and the moisture content of the atmosphere at its  
235 lowest. The minimum occurs during the monsoon, when increased cloud cover and humidity  
236 greatly increase the downwelling longwave flux. The shape of the curve closely follows the  
237 variations in the range of surface temperature (daily maximum minus daily minimum) as  
238 measured by the IRT at Niamey, and shown in Figure 12). In fact the correlation is strong  
239 enough that a simple linear function of the temperature range can predict the net LW flux  
240 with an rms error of less than  $14\text{Wm}^{-2}$ . A discussion of the main factors that control these  
241 fluxes is contained in Slingo et al. (2008).

242 The mean difference in the net flux between the two sites is just  $0.3\text{Wm}^{-2}$ , and the root mean  
243 square difference is  $6.8\text{Wm}^{-2}$ , less than the mean difference in either upward or downward  
244 fluxes. The  $7.5\text{Wm}^{-2}$  difference between the sites is consistent for both upward and  
245 downward fluxes: it is on average the same for daytime and night-time fluxes, and shows no  
246 significant variation with season. This is strong evidence of a modest calibration problem at  
247 the secondary site for at least the downwelling fluxes.

### 248 **2.3 Cloud Cover**

249 Clouds can be detected reliably during the day from the SEVIRI instrument, as described in  
250 Slingo et al (2008). We took the cloud flags for the 5 by 5 block of SEVIRI pixels centred on  
251 each AMF site, to give an estimate of fractional cloud cover every 15 minutes. A daily  
252 weighted average was taken: the weights were zero for any time period between 1800 UT and  
253 0600 UT, one for 12 noon, and varying linearly between 0600 and 1200, and between 1200  
254 and 1800. Effectively, a triangle shaped filter is run over the cloud estimates that cover  
255 daylight. This gives a cloud index which is more closely related to solar irradiance than a  
256 simple average would be, but also eliminates certain biases that are seen in the cloud product  
257 when the sun is low in the sky. The annual average of this cloud index is 0.301 at BAN, and  
258 0.314 at NIA, some 4% higher, so at least some of the higher mean irradiance at the BAN site  
259 may be explicable in terms of the lower cloud cover there.

---

## 260 **2.4 Monthly Averages**

261 Monthly statistics for downward fluxes at both sites, and for the difference between them, are  
262 summarised in Table 3. In this table  $N_d$  denotes the number of days' fluxes that were  
263 available for the statistics, s.d. denotes the standard deviation, and the units are  $Wm^{-2}$ . We see  
264 a tendency for the longwave fluxes to be most variable when the shortwave variability is  
265 relatively low, and vice versa. The SW variability is largely determined by variations in the  
266 extent and timing of cloud cover (although some will be due to aerosols), and is therefore  
267 greatest in the monsoon season at the time of the largest diurnal changes in cloud cover.  
268 Strangely, the greater variability in longwave irradiance in the winter months is probably also  
269 due to cloud cover. In dry conditions, small amounts of cloud tend to have a larger effect on  
270 the longwave flux than on the shortwave flux. In humid and cloudy conditions the  
271 emissivity of the clear sky is similar to that of the clouds, so varying amounts of cloud then  
272 have less effect on the downwelling longwave flux.  
273

---

### 3 SAMPLING UNCERTAINTY

274

275 Our overarching concern is to characterise the difference between the net radiative flux at the  
276 AMF, which is used in divergence calculations, and that which applies across the larger area  
277 which contains the measurement site: in our case a given square 50km on a side. The  
278 downwelling fluxes are modulated by cloud cover, and this is a factor that is essentially  
279 independent of the position of the instrumentation site. The changes in irradiance at a point  
280 can be quite fast (within seconds in the case of a cloud passing across the sun) but the  
281 randomness of inhomogeneities in the atmosphere, and their advection to and from the site,  
282 gives us confidence that the time-integrated irradiance at the AMF is a good estimate of the  
283 time integrated irradiance over a nearby area, provided that area is small enough and the  
284 period of integration long enough. Therefore, we will assume that variations in irradiance  
285 across the area are indeed random - no one part of it is more likely to be cloudy than any other  
286 part, say - so that if the irradiance is regarded as a random variable the point measurement and  
287 its corresponding area average have the same expected value. While there may be no bias in  
288 the downwelling terms, there will generally still be a difference between the point and areal  
289 values over any given period of time, and the best we can hope to do here is characterise the  
290 expected mean-square difference between the two values. We cannot estimate this precisely,  
291 but the existence of the second set of measurements at Banizoumbou helps us to place bounds  
292 on that variance. This forms only a part of the sampling uncertainty, being concerned only  
293 with the irradiances (although a large part, as we will see). Other factors controlling the  
294 surface radiation budget (SRB) vary much more slowly in time. These arise from surface  
295 heterogeneity and are shortwave albedo, long-wave bulk emissivity and the surface  
296 temperature. These can vary quite markedly on scales much smaller than the scale of the  
297 GERB footprint. The second set of surface flux measurements is of very limited help here,  
298 and we must exploit other sources of information to estimate the corresponding sampling  
299 uncertainties.

#### 300 **3.1 Modelling the Sampling Error**

301 Let us consider first the shortwave contribution to the SRB. This is:

302 
$$F_{SW}^{\downarrow} - F_{SW}^{\uparrow} = F_{SW}^{\downarrow}(1 - a) \qquad \text{Equ. 1}$$

---

303 where  $a$  is the albedo (this is essentially a definition of that quantity). At any given point the  
304 surface will have distinctive spectral variation to its reflectance properties, and the surface is  
305 not usually Lambertian, so the albedo generally varies with the directional distribution of the  
306 irradiance, the spectral distribution of the irradiance, and under the clearest skies will vary  
307 with time of day, and the daily average will therefore vary with time of year. There is also  
308 some variation with soil moisture content - wet soil is darker than dry soil - so the albedo may  
309 change more quickly in the monsoon season than during the dry season. Despite these  
310 considerations, the daily albedo (the average of the total reflected SW flux to the total SW  
311 irradiance) changes little from day to day during the dry season at either of the AMF sites and  
312 so can be considered a stable parameter which varies mainly with position. However, that is  
313 not the case throughout the year. Figure 13 plots the daily albedo at NIA (i.e. the ratio of the  
314 all-day reflected flux to the all-day shortwave irradiance), and shows a smoothed version  
315 through it. Month-by-month statistics for the mean value, and mean-square deviation from  
316 the smoothed curve are shown in table 4. The above-average spike at the beginning of March  
317 occurred during a notable dust storm (Slingo et al, 2006). During this period, the direct solar  
318 illumination dropped to near-zero, and almost all the shortwave irradiance was diffuse; Slingo  
319 et al. (2006) stress the higher uncertainty of the shortwave fluxes at this time. It would be  
320 surprising if, during this severe dust storm, there were not some deposition of dust on the  
321 upward pointing pyranometers, which would have the effect of raising the apparent albedo.  
322 The sharp dip at the beginning of June happens in the middle of a four day rain event, and the  
323 variability in albedo during the remainder of the monsoon is probably driven by variations in  
324 soil moisture. Table 5 shows the same statistics for the auxiliary site. The variability in  
325 albedo from month to month at either site is quite well correlated ( $r>0.8$ ) with the mean  
326 monthly rainfall. The small variations during the dry season are possibly derived from  
327 instrumental uncertainties, but the albedo varies somewhat with the proportion of diffuse  
328 irradiance, and so some variability can be expected from the variability in that proportion.  
329 The small variation seen in the dry seasons is consistent with the small differences in the  
330 MODIS white-sky (100% diffuse) albedo and black-sky (0% diffuse) albedo products.

331 The longwave upward flux consists of reflected downward flux, as for the shortwave, and the  
332 radiative flux emitted by the ground. Simple parameterizations of the instantaneous values of  
333 these terms are given respectively by:

334  $(1 - \epsilon)F_{LW}^{\downarrow}$  and  $\epsilon T_s^4$

---

335 where  $T_s$  is the surface temperature and  $\varepsilon$  the emissivity (so that  $1-\varepsilon$  is the longwave albedo).

336 These expressions are correct for a grey Lambertian surface. The instantaneous net flux is:

$$337 \quad SRB = F_{SW}^{\downarrow} - F_{SW}^{\uparrow} + F_{LW}^{\downarrow} - F_{LW}^{\uparrow} \quad \text{Equ. 2}$$

338 or, using the expressions given above,

$$339 \quad SRB = F_{SW}^{\downarrow}(1-a) + \varepsilon(F_{LW}^{\downarrow} - \sigma T_s^4) \quad \text{Equ. 3}$$

340 and the net surface fluxes used in our divergences studies are these values, integrated over a

341 24 hour period. To simplify the notation, the variable  $g$  will be used for the daily average of

342  $\sigma T^4$ ;  $g$  is the upwelling blackbody flux for the given temperature time series. We will use  $S$

343 and  $L$  for the short-wave and longwave time-averaged irradiances, a subscript  $N$  to denote

344 value obtained at the main AMF site, a subscript  $B$  to represent any flux measured at the

345 auxiliary site, and a subscript  $A$  to denote an average of the variable over the appropriate

346 GERB footprint. Then our observation of the daily mean flux, and what we really should be

347 using to combine with the TOA fluxes are:

$$348 \quad SRB_N = S_N(1-a_N) + \varepsilon_N(L_N - g_N) \quad \text{and} \quad SRB_A = S_A(1-a_A) + \varepsilon_A(L_A - g_A) \quad \text{Equ. 4}$$

349 respectively. We denote by  $U$  the arithmetic difference of these two, which represents the

350 uncertainty associated with the limited sampling, which we may also call the sampling error.

351 We split  $U$  up into the sum of 5 terms,  $U_1$  to  $U_5$ :

$$\begin{aligned} 352 \quad U_1 &= (S_N - S_A)(1-a_N) & U_2 &= S_A(a_A - a_N) \\ U_3 &= \varepsilon_N(L_N - L_A) & U_4 &= \varepsilon_N(g_A - g_N) \\ U_5 &= (\varepsilon_N - \varepsilon_A)(L_A - g_A) \\ U &= SRB_N - SRB_A = U_1 + U_2 + U_3 + U_4 + U_5 \end{aligned} \quad \text{Equ. 5}$$

353 Each of these 5 terms is the product of a difference between some quantity and its area

354 average, times some parameter value at the AMF, or times an area averaged-flux.

355 Specifically:  $U_1$  is the contribution to the uncertainty of variability in shortwave irradiance

356 across the area of interest, and  $U_2$  that from the difference in the surface albedo at the site and

357 the average albedo across the GERB footprint.  $U_3$  results from spatial variations in

358 downwelling longwave flux,  $U_4$  from spatial variations in surface temperature, and  $U_5$  the

359 result of systematic difference in emissivity. It is done this way in the hope that these five

---

360 terms will have some statistical independence, and that we can understand the greater part of  
361 the sampling uncertainty by understanding the corresponding problems for these five terms.  
362 In practice, there is some correlation between these terms which in practice generally acts to  
363 reduce the error slightly.

### 364 **3.2 Irradiance Uncertainties**

365 It is in estimating the mean square values of  $U_1$  and  $U_3$  that the value of the second AMF suite  
366 of radiation instruments proves most valuable. The difference in SW irradiance between the  
367 two can put an upper bound on  $U_1$  squared, and the correlation between the two sites leads to  
368 another estimate which is smaller, and perhaps more optimistic, but which imposes slightly  
369 more restrictive assumptions in the irradiance field. The same applies to  $U_3$ .

#### 370 **3.2.1 A possible lower bound to the irradiance uncertainty**

371 For one estimate of the sampling uncertainty we can use a result from Settle (2004), where an  
372 expression was derived for precisely this quantity, under certain constraints. These amount to  
373 assuming that the irradiance as a random variable with a mean and variance independent of  
374 position, and an autocorrelation structure that is a function only of the distance between two  
375 points, divided by a scale length. The expression, in terms of integrals of the autocorrelation  
376 function, was derived for the case when the comparison point is located at the centre of a  
377 square area. The required expression is:

$$378 \quad \mathcal{E}\{(F_N - A_N)^2\} = -2\gamma'(0) \frac{D}{R} \left( \frac{2\sqrt{2}-1}{15} \right) V; \quad \text{Equ. 6}$$

379 where  $V$  is the variance of  $F$  at a point,  $\gamma\left(\frac{r}{R}\right)$  is the spatial autocorrelation function (assumed  
380 isotropic) of  $F$  at distance  $r$ ,  $D$  is the length of the side of the area  $A$ , and  $R$  ( $\gg D$ ) is the  
381 autocorrelation length, defined such that:

$$382 \quad \int_0^\infty t\gamma(t)dt = 1 \quad \text{Equ. 7}$$

383 We will see that the correlations ( $\rho$ , say) are indeed very high between the two sites, so we  
384 have, expanding the correlation function out to first order:

---

385  $\rho = \gamma\left(\frac{L}{R}\right) \cong 1 + \frac{L}{R}\gamma'(0)$  Equ. 8

386 where  $L$  is the distance between the two measurements. Therefore:

387  $\gamma'(0) = -\frac{R}{L}(1-\rho)$  Equ. 9

388 so that:

389  $\mathbb{E}\{(F_N - A_N)^2\} = 2(1-\rho)\frac{D}{L}\left(\frac{2\sqrt{2}-1}{15}\right)V = 0.24(1-\rho)\frac{D}{L}V$  Equ. 10

390  $V$  and  $\rho$  are measured, and  $D$  and  $L$  are known. In practice the distance  $L$  between the sites is  
 391 53 km,  $D=50$ km for the GERB pixel.

392 The numerical constant, 0.24, appearing in Equ. 10 holds for point measurements made at the  
 393 centre of a bounding square. The AMF sites are not exactly located at the centres of the  
 394 GERB pixels containing them, and the numerical constant will be slightly greater than this. If  
 395 the distance,  $d$  say from the AMF to the true centre of the corresponding GERB footprint is  
 396 modest, then the necessary adjustment is that the constant increases from 0.24 to  
 397  $0.24+1.76(d/D)^2$ .

### 398 **3.2.2 An upper bound to the irradiance uncertainty**

399 There must be some doubt that the assumptions inherent in the just-derived estimate of  
 400 sampling uncertainty are fully realised. The stationarity implicit in Settle's 2004 derivation is  
 401 evidently not well honoured through the year, as there are minor differences in the mean  
 402 irradiance at the two sites (Figure 4); the assumption of an isotropic autocorrelation function,  
 403 that depends on a single scale parameter, is unproven, and a small correction is needed to  
 404 account for the off-centre locations of the flux stations. The estimate we have derived above  
 405 is likely therefore to be on the optimistic side. However, the following argument gives us an  
 406 upper bound to the sampling error, which gives a larger estimate than the one we have just  
 407 derived, but not greatly so. We can relax the requirement of global stationarity, and need  
 408 assume nothing about the autocorrelation structure. Our main assumption is that the  
 409 measurement at either site be an unbiased estimate of the corresponding area average.

410 That upper bound to the variance is half the mean square difference between the values at the  
 411 two sites. To see this, let the time-averaged fluxes at the two sites, Niamey and  
 412 Banizoumbou, be denoted by  $F_N$  and  $F_B$  respectively. Consider areas based on each of these:  
 413 let the spatial average of the corresponding time-averaged fluxes over those areas be  $A_N$  and  
 414  $A_B$ . We are interested in the mean square difference between  $F$  and the corresponding  $A$ , and  
 415 we can relate it to the observed flux difference thus:

$$\begin{aligned}
 (F_N - F_B)^2 &= (F_N - A_N - F_B + A_B + A_N - A_B)^2 \\
 416 \quad &= (F_N - A_N)^2 + (F_B - A_B)^2 + (A_N - A_B)^2 + 2(A_N - A_B)(A_B - F_B) \\
 &\quad + 2(A_N - A_B)(F_N - A_N) - 2(F_N - A_N)(F_B - A_B)
 \end{aligned}
 \tag{Equ. 11}$$

417 We now treat the differences in a statistical manner, replacing each term with its expectation.  
 418 Statistically,  $\mathcal{E}(F) = A$ , so the fourth and fifth terms on the right hand side can be set to zero.  
 419 The last term is also essentially zero, as it makes no sense for point values at the two sites to  
 420 be consistently both higher or lower than their respective area averages. So, applying  
 421 expectations, we have:

$$\mathcal{E}\{(F_N - F_B)^2\} = U_N^2 + U_B^2 + \mathcal{E}\{(A_N - A_B)^2\} \geq U_N^2 + U_B^2
 \tag{Equ. 12}$$

423 where  $\mathcal{E}$  denotes expectation value. Taking  $U_N \sim U_B$  we have the following formula for the  
 424 mean squared uncertainty:

$$\mathcal{E}\{(F_N - A_N)^2\} = U_N^2 \sim \frac{1}{2} \mathcal{E}\{(F_N - F_B)^2 - (A_N - A_B)^2\} \leq \frac{1}{2} \mathcal{E}\{(F_N - F_B)^2\}
 \tag{Equ. 13}$$

426 say. Replacing  $\mathcal{E}\{(F_N - F_B)^2\}$  with observed values gives us the required upper limit.

427 The usefulness of this limit depends on the magnitude of the mean square difference between  
 428 the two area-averaged fluxes (i.e.  $(A_N - A_B)^2$ ). The smaller the areas, the more likely those area  
 429 averages are to be different, the greater their mean square difference, and the more pessimistic  
 430 and less valuable the derived upper limit. The estimate is most accurate when the areas are  
 431 large, and the expected difference between two area averages much smaller than the sampling  
 432 error on either. However, if the areas are too large, and overlap significantly, then we are no  
 433 longer justified in ignoring the term in Equ. 14 containing  $(F_N - A_N)(F_B - A_B)$  which effectively  
 434 approaches the flux correlation between the two sites. The size of the GERB pixel is

---

435 comparable to the distance between the two sites, so for this specific case there would be no  
436 overlap, the upper limit is valid, and some difference can be expected between  $A_N$  and  $A_B$ ,  
437 although this is difficult to quantify without a model for the spatial variability in irradiance.

438 For genuinely random fields with the appropriate autocorrelation structures, the upper bound  
439 to the sampling error variance given by Equ. 11 is about four times that implied by Equ. 10  
440 (so that the associated flux uncertainties differ by a factor of about 2). We will call these the  
441 pessimistic and optimistic estimates, respectively, of the relevant contribution to the sampling  
442 uncertainty. We will later use a value of 3/4 of the upper limit, midway between the  
443 optimistic and pessimistic estimates, as our preferred estimate of the true uncertainty. Despite  
444 being based on time series at just two locations, it is unlikely to be far from the real sampling  
445 uncertainty.

446 These arguments can only be applied to the downwelling fluxes, as they require the AMF  
447 value to be an unbiased estimate of the area average to simplify the arithmetic. This simply  
448 isn't true for the remaining terms, which depend on surface variability that may have much  
449 shorter correlation length scales, and for which time-averaging is of no benefit.

## 450 **4 QUANTIFYING THE SAMPLING UNCERTAINTY IN RADAGAST**

### 451 **4.1 Bias and Mean Square Uncertainty**

452 In the previous section we decomposed the sampling error, the difference between the  
453 observed net surface flux observed at the AMF, and the average of the same quantity over the  
454 GERB footprint, into five separate terms. Of these terms those,  $U_1$  and  $U_3$ , that are  
455 proportional to the differences in irradiance have, regarded as random variables, expectation  
456 zero, as (we have assumed that) the irradiance measured at the AMF is an unbiased estimate  
457 of that over the GERB square. The remaining terms, each dependent on the difference  
458 between a point value of some surface variable and its area average, represent possible  
459 sources of bias. Ignoring  $U_4$  for now, we can combine the remaining bias terms thus:

$$460 \quad S_A(a_A - a_N) + (\varepsilon_N - \varepsilon_A)(L_A - g_A) \quad \text{Equ. 15}$$

461  $S_A$  is generally between 200 and 250Wm<sup>-2</sup>, and the term  $g_A - L_A$  about 100Wm<sup>-2</sup>, so provided  
462 the emissivity and albedo at the AMF site are not more than about .02 different from the  
463 corresponding area average, these contributions to the bias should be less than 5Wm<sup>-2</sup>.

464 However, as we shall see, while any bias in the emissivity term is likely to be small, it seems

---

465 that the difference between the albedo of the immediate area of the AMF, and that of the  
466 GERB pixel as a whole, could be about 0.04, with the GERB value being the higher. This  
467 term alone could thus introduce a systematic error of 8-10Wm<sup>-2</sup> into our calculations of the  
468 SRB.

469 The remaining term,  $U_4$ , effectively the difference between  $g$  at the AMF and averaged over  
470 the GERB footprint, is more difficult to assess. As will later be shown, it appears from  
471 satellite data that the variability in  $g$  across the GERB area may be no more than a few Wm<sup>-2</sup>  
472 under clear skies (as will be shown later). The combined effect is a bias that is probably  
473 limited to less than 10Wm<sup>-2</sup> for the daily average of the net surface flux. We will return to  
474 this in the relevant section below.

475 The bias may be small, but the day-to day variability need not be small if the variance of the  
476 unbiased terms,  $U_1$  and  $U_3$  should be large. The mean square uncertainty is:

$$477 \quad U^2 = U_1^2 + U_2^2 + U_3^2 + U_4^2 + U_5^2 \quad \text{Equ. 16}$$

478 assuming that there is no significant correlation between the individual components. In fact,  
479 there is some correlation, which generally tends to lower the uncertainty. For example,  
480 variations in cloud cover tend to affect the irradiances differently, increasing cloud cover  
481 tending to increase longwave irradiance and decrease shortwave irradiance. The effects are  
482 generally small, however.

483

#### 484 **4.1.1 Variability of Shortwave Irradiance ( $U_1$ )**

$$485 \quad U_1 = (S_N - S_A)(1 - a_N)$$

486 This is the error that arises when the shortwave irradiance measured at the instrument point is  
487 not the same as the average irradiance over the required area. In cloudy conditions short  
488 wave irradiance can vary rapidly at a point, and from point to nearby point, according to  
489 whether the sun is obscured or not. With no reason to believe that our measurement site is  
490 any more or less cloudy, on average, than anywhere else in the GERB footprint, the AMF  
491 value,  $S_N$ , is taken to be an unbiased estimate of the required value,  $S_A$ , while the factor  $(1 - a_N)$   
492 will be regarded as essentially constant over a period of weeks. The mean square difference  
493 of  $S_N - S_A$  we bound using the methods described earlier. The contribution  $U_1$  is then about

---

494 three-quarters of the uncertainty on  $SW\downarrow$  once the albedo contribution has been factored into  
495 the calculation. Over the whole of 2006, the mean square difference between the daily  
496 average of  $SW\downarrow$  at the two sites is  $222 \text{ (Wm}^{-2}\text{)}^2$ . Halving this, and taking the square root gives  
497 an uncertainty, from this source alone, of  $10.5\text{Wm}^{-2}$  on the daily average, which is  
498 considerably larger than the presumed bias in the measurement. The corresponding error  $U_1$   
499 is then about  $7\text{Wm}^{-2}$  when we include the albedo.. As our preferred estimate of irradiance  
500 uncertainty is three-quarters of the upper bound, our overall estimate of uncertainty is about  
501  $5\text{Wm}^{-2}$  in the shortwave. But this is an average over the whole year of course; this upper  
502 bound will be higher when there is plenty of cloud about, and lower in cloud -free conditions.  
503 Taking just the months of January and February, for example, we find the mean square  
504 difference in  $SW\downarrow$  to be  $22.6 \text{ (Wm}^{-2}\text{)}^2$ , giving an upper limit to the root mean square error for  
505  $U_1$  of just  $2.5\text{Wm}^{-2}$  and a preferred estimate of  $2\text{Wm}^{-2}$ .

506 Estimates of the error, based on the monthly mean albedo and monthly statistics of the flux  
507 differences between the sites, are shown in Table 9. The day-to-day correlation of the  
508 shortwave irradiance, after allowing for the seasonal trend, is very small, so averaging over  $N$   
509 days will reduce this uncertainty by a further factor  $\sqrt{N}$ .

#### 510 **4.1.2 Spatial Variability in albedo ( $U_2$ )**

$$511 \quad U_2 = S_A(a_A - a_N)$$

512 The second source of error, according to the simple view (Equ. 5), is the fact that the arbitrary  
513 siting of the radiometers means the albedo folded into the measurements of reflected flux is  
514 almost certainly different from the mean albedo of the larger area, which is the quantity  
515 relevant for estimating divergence. Because the effect is systematic, it is not possible to use  
516 the two data sets to estimate the scale of the error, and in fact no ARM measurements are  
517 useful for such a purpose. We must use some other source of data to examine the spatial  
518 variability. The most sensible option seems to be the estimates of surface albedo generated  
519 from the Terra and Aqua missions (Schaaf et al., 2002), given their high spatial resolution and  
520 the significant amount of development, validation and testing that has been devoted to that  
521 product. In the first instance we will not aim for a direct comparison of the surface albedos  
522 formed from the point fluxes with those in the satellite product. Instead, we try to assess how  
523 the satellite albedo inferred for the immediate vicinity of the AMF compares to that inferred

---

524 for the GERB pixel, found by averaging over the many MODIS pixels that fit into a GERB  
525 pixel.

526 For the period of interest, the available products correspond to various spectral and broad-  
527 band albedos evaluated over 16 day periods, at 500m spatial resolution (version 5). They are  
528 generated every 8 days, so there is some oversampling of the daily MODIS data. There are  
529 ten thousand such estimates within each GERB footprint, and the observed variability of  
530 those albedo estimates can be used to characterise the heterogeneity of the reflected fluxes at  
531 sub-GERB scale. The MODIS albedo product in fact consists of much more than a single  
532 number, as it gives spectral albedo over a number of wavelengths regions, allows calculation  
533 of albedo at different times of day (different values of solar zenith angle) and also  
534 distinguishes between a black-sky albedo (that which would apply in the complete absence of  
535 diffuse irradiance) and a white-sky value, which assumes that the irradiance is completely and  
536 uniformly diffuse. In practice, the numerical difference between these values is small, and a  
537 “blue-sky” albedo, which lies between them, will not vary much from either. For the sake of  
538 estimating heterogeneity, and the typicality of the AMF locations, we have taken the black-  
539 sky, broad-band albedo evaluated at local solar noon.

540 Table 6 shows the mean MODIS-derived albedo for GERB pixels containing the two sites,  
541 the variability of the MODIS albedo within the GERB pixel (the standard deviation of the  
542 retrieved albedos of up to 10,000 MODIS pixels) and the albedo of the MODIS pixel that  
543 contains the instrument site. In Figure 15 the difference between the latter value and the area  
544 average is plotted, and the standard deviations drawn on. The auxiliary site appears to be a  
545 faithful representative of the GERB pixel which contains it, but the MODIS albedo for the  
546 500m square containing the main AMF is significantly different from the mean of the GERB  
547 pixel (consistently different by about .04, and more different than 1 standard deviation at all  
548 times).

549 The BAN site is clearly typical of the surrounding area, perhaps more than we have a right to  
550 expect, as the difference in the albedo values, BAN pixel and GERB pixel, are usually only a  
551 fraction of the scatter observed in the GERB pixel. The 500m X 500m area around the main  
552 site, however, is clearly not so typical of other similar subdivisions of the corresponding  
553 GERB pixel, or the area as a whole. Had we chosen such a point at random, the albedo error  
554 would have a standard deviation of about .025 (and a mean of zero, of course), whereas the  
555 actual site is different by 1½ to 2 times this. If the few square metres seen by the pyranometer

---

556 measuring upward flux should be typical of that 500m square area, then there is a bias of  
557 some 8-12Wm<sup>-2</sup> applying to the shortwave radiation budget at the main site.

558 All this assumes that the spatial variations in the MODIS albedo product are a reliable guide  
559 to the true variability on the ground. We can see that they are, at least for one day in January  
560 2006, by comparison with albedo measurements from a low-flying aircraft. We compare the  
561 MODIS albedo calculated for the 16 day period between January 16th and January 31st,  
562 2006, with albedos obtained from a flight on the 19th January 2006 of the Facility for  
563 Airborne Atmospheric Measurements (FAAM), run jointly by the UK's Natural Environment  
564 Research Council and the UK Met Office during the DABEX campaign (Haywood et al,  
565 2008). The flight took place between the vicinity of the NIA site (1040 UT) and the BAN site  
566 (1050 UT), at a height of 500 ft. Upwelling and downwelling broadband fluxes were recorded  
567 every second. Given the speed of the aircraft, these measurements overlap heavily and there  
568 might be up to four FAAM albedo measurements for each MODIS pixel on the transect. The  
569 albedos at the start and end of the flight agree quite well with the corresponding AMF  
570 albedos, and are rather higher than the MODIS values. This applied along the length of the  
571 transect, but consistently so: if the MODIS black-sky albedos for this period are multiplied by  
572 1.1352, they fall nicely into line with the FAAM values (Figure 14).

573 The good match of the fine detail gives us a lot of confidence that the MODIS albedo product  
574 can be used to identify how typical the locality of the AMF is for the much larger GERB area.

575 We have concentrated here on characterising the spatial variability of the albedo, assumed  
576 more-or-less constant over the 8 day period of the MODIS retrievals. As we saw in section  
577 3.1, this appears to be a good assumption during the dry seasons, although less so during the  
578 monsoon (at which time, in addition, the MODIS retrieval struggles to find enough cloud-free  
579 data to generate its albedos).

### 580 **4.1.3 Variability in longwave irradiance $U_3$**

581 
$$U_3 = (L_N - L_A)\epsilon_N$$

582 The longwave irradiance term can be treated in a manner similar to that used for  $U_1$ . We shall  
583 assume that there is a flat calibration offset of 7.5Wm<sup>-2</sup> to be applied to the flux difference;  
584 when this is done, the average over the year of the squared difference in LW↓ is (3.3Wm<sup>-2</sup>)<sup>2</sup>,  
585 giving an upper limit of  $3.3\div\sqrt{2} \sim 2.3\text{Wm}^{-2}$ . From Table 7 we see that the variance of this flux

---

586 is generally much smaller than that for the shortwave, while the correlation is higher. These  
587 factors mean that our two bounds for longwave irradiance are very small: the error based on  
588 the correlation is never more than  $2\text{Wm}^{-2}$ , which is probably within the accuracy of the  
589 pyrgeometer. The largest monthly error value that we derive is the upper limit applied to the  
590 April fluxes; this is just  $3.45\text{Wm}^{-2}$ .

#### 591 **4.1.4 Variability in emissivity $U_5$**

592 This term is given by:

$$593 \quad U_5 = (L_A - g_A)(\epsilon_N - \epsilon_A)$$

594 The mean net flux at BAN is  $101\text{Wm}^{-2}$  (with a scatter of  $27\text{Wm}^{-2}$ ) so every .01 uncertainty in  
595 emissivity translates into a systematic error of  $1\text{Wm}^{-2}$  or so in the LW uncertainty. The root  
596 mean square variation in emissivity can never be less than half the range in its values, and  
597 these sensibly lie between about 0.9 for bare rock and .98 for water. This sets an upper limit  
598 of about 0.04 to the  $1\sigma$  error in emissivity (the real value will probably be lower still) and so  
599 an upper limit of about  $5\text{Wm}^{-2}$  to this systematic component of the longwave sampling  
600 uncertainty. The true value (which contributes to the bias in our estimate of the SRB) is  
601 likely to be smaller than this.

602 Satellite-derived estimates of emissivity are very rarely produced, although reasonable  
603 knowledge of spectral emissivity is required to estimate land surface temperature from  
604 satellite infra-red measurements. To estimate the variability of emissivity in our study we  
605 took data from the global IR land surface emissivity database (Seemann et al., 2008). This  
606 has a 5km resolution, and is available as monthly global data. The statistics of these values  
607 for January and September 2006, for the GERB pixel containing the NIA station, are given in  
608 Table 8.

609 The variability of the emissivity - a scatter value of .003 or so - means that there is probably  
610 no significant contribution to the sampling error from this source. It could be that the  
611 emissivity varies more appreciably at scales below that of the 5km dataset, but that is beyond  
612 the scope of our investigation.

#### 613 **4.1.5 Variability in blackbody ground flux $U_4$**

$$614 \quad U_5 = \epsilon_N(g_A - g_N)$$

---

615 For this we can reasonably assume the emissivity is equal to the area value of 0.935 from the  
616 land surface emissivity database (previous section) and just work with the variability of the  
617 blackbody flux,  $g$ . This component of the SRB uncertainty is the most difficult to  
618 characterise with the observations from the AMF sites. In the first instance, we strictly  
619 speaking have no observations of the surface (skin) temperature at all, although at the main  
620 site an infrared thermometer (IRT), which covers the 8-13 $\mu$ m atmospheric window, is used to  
621 calculate an approximation to the required value (see also Bharmal et al., 2008). Under clear  
622 skies the downwelling flux in this window is relatively small, and so the reflected  
623 contribution to the measured flux is the product of two small amounts and can be neglected.  
624 The temperature value determined still has some assumptions about the local spectral  
625 emissivity folded into it. These numbers are available only at the main site, and not at the  
626 auxiliary site, so we can construct just one time-series of  $g$ . We could use MODIS  
627 temperature retrievals, which give spatial images of temperature fields twice a day, with an  
628 eight day product also defined, to try to characterise the spatial variability of  $g$ , but this must  
629 entail some assumptions about the actual shape of  $g$  as a function of time of day. The MODIS  
630 temperatures are more suited towards mitigating the effects of spatial heterogeneity for  
631 radiative transfer calculations at the appropriate time of day (Bharmal et al., 2008). These high  
632 resolution maps of surface temperatures can only be derived in the absence of cloud cover,  
633 and assumptions still need to be made about the surface spectral emissivity. With these  
634 caveats in mind, we shall nevertheless try to estimate the variability of  $g$  from satellite data.

635 Retrievals of land surface temperature can be made from a number of satellites using so-  
636 called 'split window' algorithms (e.g. Price 1984, Becker and Li 1990, Sobrino and  
637 Romaguera 2004), but for most the number of temperature maps thus obtained is woefully  
638 short of the number needed to make a decent estimate of the daily average of temperature's  
639 fourth power. SEVIRI, however, takes 96 sets of thermal images each day, once every 15  
640 minutes, and the LandSAF (Land Surface Analysis Satellite Applications Facility,  
641 <http://landsaf.meteo.pt/>) generates estimates of land surface temperature at each of these  
642 times, in a product that has 5km ground resolution. Of course, cloud cover affects one's  
643 ability to recover surface temperature, and there are many gaps in this temperature product.  
644 Sometimes these are spatially very extensive, as when there is large-scale cloud cover or an  
645 image acquisition failed; at other times the drop-outs are patchy. The cloud clearing  
646 algorithm appears to be very conservative, as there are extremely few days where a complete  
647 run of 96 temperatures are obtained over most of the area.

---

648 **16 December, 2006**

649 One such clear day was 16th December, when 85 of the 90 pixels had full temperature sets of  
650 96 values (the remaining 5, which are always missing in these data sets at this time, have  
651 probably been masked out as being ‘water’ rather than ‘land’). The time series of  $g$  for  
652 temperatures retrieved for the 5km SEVIRI sample containing the AMF was compared to the  
653 values of  $g$  derived at 15 minute intervals using the IRT temperatures. The comparison of  
654 temperatures is shown in (Figure 16a), the match up of the corresponding black body flux in  
655 (Figure 16b). The value of  $g$  for this day is 464.6, calculated from the IRT temperatures. That  
656 for the 5km cell containing the AMF is 460.9, a difference of  $3.7\text{Wm}^{-2}$ .

657 The hour-to-hour differences seen may well be real of course, as the SEVIRI retrieval is  
658 generated for a 5km by 5km square area, while the IRT sees just a few square metres of soil.  
659 The SEVIRI temperature includes contributions from vegetation, but also from airport  
660 buildings and runways. For each of the 96 images the mean and standard deviation of  $\sigma T^4$   
661 were calculated, and are plotted in Figure 17 (the mean data are the solid black curve, the  
662 green curves correspond to the mean curve  $\pm 1$  sd. and the values for the pixel containing NIA  
663 are shown as dots). The cell containing the NIA site lines up quite well with the mean curve  
664 of all the cells; the average daily flux ( $g$ ) for the NIA cell is  $460.9\text{Wm}^{-2}$  and that for the mean  
665 curve is  $459.0\text{Wm}^{-2}$ . When we calculate  $g$  for all of the 85 cells in the December 16 set, we  
666 find the standard deviation is just  $3.2\text{Wm}^{-2}$  (the mean is still 459, of course). This suggests  
667 that the NIA cell is very typical of the GERB footprint as a whole; the difference in  $g$  between  
668 the NIA cell and the GERB mean is just 0.6 of a standard deviation of the SEVIRI values.

669 The curves in Figure 17 corresponding to the mean flux  $\pm$  one sd are based on statistics at  
670 each of the 96 timesteps; the fluxes  $g$  corresponding to the two green curves are more  
671 different than two standard deviations of the set of 85  $g$  values. The maximum and minimum  
672 curves do not correspond to the fluxes of actual 5km samples.

673 Whether the AMF data provide a good representation of what is happening in the NIA cell is  
674 a more subtle question, but the reasonable correspondence in  $g$ , despite the difference in the  
675 range of temperatures seen (Figure 16), suggests it is, at least for the daily averages we are  
676 considering here. We can get down to slightly better resolution by using the SEVIRI data  
677 themselves, and a very simple split-window estimate of the land surface temperatures:

$$678 \hat{T}_s = aT_{10.8} + (1-a)T_{12.0} \quad \text{Equ. 17}$$

---

679 where  $T_{10.8}$  and  $T_{12.0}$  are the brightness temperatures inferred for the split-window SEVIRI  
680 channels,  $\hat{T}_S$  is the estimate of LST, and  $a$  is a parameter (typically about 4 for split window  
681 algorithms). For any given value of  $a$  this allows us to generate a simulated series of surface  
682 temperatures, and hence of  $g$ , at the higher spatial resolution. Varying  $a$  from 2 to 6 makes  
683 little difference to the spatial variance of  $g$ , which is typically between 3 and 4  $\text{Wm}^{-2}$  for the  
684 361 SEVIRI pixels defining the GERB NIA pixel. Working with a block of 19 by 19 pixels  
685 that overlap the GERB pixel produces a slightly lower variance of between 3 and 4  $\text{Wm}^{-2}$  for  
686 each site. The value of  $g$  evaluated for the 3km pixel containing the AMF is within 0.2 $\text{Wm}^{-2}$   
687 for the BAN pixel, but about 1 s.d. different for the NIA pixel, that pixel being “hotter” by 3-  
688 4 $\text{Wm}^{-2}$  than the GERB area it represents. That is in the sense we would expect, as the albedo  
689 there is lower than the average, meaning more shortwave heating of the surface takes place.  
690 We will therefore assume that the area around NIA has values of  $g$  that are on average about 1  
691 standard deviation greater than the mean of the corresponding GERB pixel.

692 At other times in the year, where all 96 temperature estimates were available over most of the  
693 area, the variability in the daily average of  $T^4$  was relatively small. However, these occasions  
694 were in the dry season, and no useful complete sequences were available during the monsoon  
695 period. To extend the number of temperature sets significantly the following approach was  
696 taken. For any given day, for each of the 90 SEVIRI 5km by 5km cells for which LST was  
697 generated, the number of error-free, cloud-free estimates was counted. If this was greater  
698 than a certain threshold, then any missing values would be estimated by interpolation, and the  
699 time average then taken. The number of true values employed is used to define a simple  
700 confidence parameter for the estimate: it is zero when the number of true values is at the  
701 threshold for acceptance, is one if all 96 temperature values exist, and otherwise varies  
702 linearly. For example, if the threshold is 60, an estimate generated from a set of 78 (halfway  
703 between 60 and 96) retrieved temperatures has an assigned confidence value of 0.5 for that  
704 pixel. This process gives up to 90 estimates of the daily average of  $\sigma T^4$  across the GERB  
705 pixel: the standard deviation of these numbers is taken as the sampling uncertainty, and the  
706 average confidence parameter is calculated as an uncertainty parameter on that sampling  
707 uncertainty.

708 Figure 18 shows the standard deviation in the daily average of  $\sigma T^4$  around Niamey when the  
709 threshold for a calculation is that 60 of the 96 possible LST values should exist. Blue dots in  
710 this plot represent sampling error calculations for which the confidence parameter is higher

---

711 than 80%. The red dots are for those that have confidence values less than 0.2, and the open  
712 circles represent the in-between values. During periods of low cloud cover, at either end of  
713 the year, this uncertainty is seen to be no more than about 3-4  $\text{Wm}^{-2}$ . There appears to be a  
714 slight dependence on season of the spatial variability of  $g$ ; the blue symbols in the middle of  
715 the year being a little higher than at the beginning and end of the year, but we find that any  
716 calculations that suggest the scatter could be more than about  $7\text{Wm}^{-2}$  are those in which we  
717 have least confidence. When we have most confidence in our calculation of sampling error,  
718 that error is smaller. This may reflect upon the interpolation method chosen, or it may indeed  
719 be the case that in cloud-free conditions, which is when we expect the confidence parameter  
720 to be high, there is little variation in the time average of  $\sigma T^4$ .

721 Evidence from the clear day of December 16, 2006 suggests that the area around Niamey is  
722 fairly typical of the larger GERB area; blackbody fluxes of the 5km area containing the AMF  
723 lie within one-half to two-thirds of one standard deviation of such sub-area fluxes, and the  
724 3km area around is similarly typical of the 15kmx15km area around it. The match between  
725 the diurnal temperature plot at the AMF and the SEVIRI estimates of temperature show  
726 discrepancies, with the SEVIRI retrieval being hotter at midday and cooler at night;  
727 nevertheless, the blackbody fluxes represented by the two time series are less than  $2\text{Wm}^{-2}$   
728 apart. Extending the evaluation from the dry season is problematic, given that cloud cover  
729 reduces the number of satellite LST estimates we have to work with. There does seem to be a  
730 tendency for the variability of  $g$  to be slightly higher outside the dry season, but that may be  
731 an artefact of the limited data available to us.

732 Working from the SEVIRI data therefore suggests that the variability in  $g$  is about  $4\text{Wm}^{-2}$  in  
733 clear sky conditions, which is rather less than we might expect given variations in temperature  
734 that are evident at any one time. The SEVIRI pixel containing the BAN site appears to be  
735 completely typical for the surrounding area for the  $g$  function, just as it is for the albedo. NIA  
736 runs a little hotter, and a bias of about  $4\text{Wm}^{-2}$  can perhaps be expected there.

## 737 **5 MONTHLY ESTIMATES OF THE SAMPLING ERROR**

738 The uncertainties estimated for each month are tabulated in Table 9. The values correspond  
739 to the AMF value, minus the corresponding area average; units are  $\text{Wm}^{-2}$ . Unsigned numbers,  
740 or those preceded with a minus sign correspond to systematic differences, while values

---

741 presented as  $\pm$  numbers represent the root mean square difference of a quantity whose  
742 systematic error is taken to be negligible.

743 To recall:  $U_1$  gives that part of the total uncertainty associated with variations in short-wave  
744 irradiance across the area of interest; it is calculated by multiplying together the observed  
745 monthly average co-albedo and three-quarters of the upper bound for the root-mean-square  
746 uncertainty of irradiance.  $U_2$  gives that associated with the difference between the albedo at  
747 the AMF and the required area average of albedo; for this we have assumed fixed albedo  
748 errors of -0.04 at NIA and +0.005 at BAN, and multiplied these by the observed mean SW  
749 irradiance.  $U_1+U_2$  gives the sampling uncertainty that is attached to the shortwave component  
750 of the surface flux.

751  $U_3$  is from variations in long-wave irradiance across the area of interest, and is calculated as  
752 three-quarters of the upper bound multiplied by 0.935, the assumed area emissivity; for BAN,  
753 an assumed calibration correction of  $7.5\text{Wm}^{-2}$  has been applied. As there is a slight  
754 compensation between uncertainties in the shortwave and longwave irradiances the combined  
755 uncertainty of  $U_1+U_3$  is also given.

756  $U_4$  gives the uncertainty which arises from variations in surface temperature, based on  
757 SEVIRI Land Surface Temperature products.  $U_5$  that which is associated with variations in  
758 emissivity; the spatial datasets of Seemann et al (2008) lead us to conclude that this term is  
759 less than  $1\text{Wm}^{-2}$ , and so is not shown in the table. The sum  $U_3+U_4+U_5$  is the sampling error  
760 for the long-wave flux.

## 761 **6 DISCUSSION**

762 Inspection of Table 9 shows that the biggest contributions to the sampling error using the NIA  
763 data are from the variability of shortwave irradiance during the monsoon period, and the  
764 systematic albedo difference during the dry seasons. The errors on the longwave contribution  
765 to the SRB are generally much less than these. The peak of the SW irradiance uncertainty is  
766 realised in August, reaching  $11\text{-}12\text{Wm}^{-2}$  (1 standard deviation). In this month there are 10  
767 days on which the observed flux difference between the two sites was at least  $29\text{Wm}^{-2}$ , and all  
768 these numbers are included in the statistics. On such days the large difference between the  
769 two sites presents us with *a priori* evidence that the daily average SW irradiance then varies  
770 significantly over a distance comparable to the ARG footprint. Similarly, days with heavy  
771 rainfall are also included, as the only criterion for inclusion in the statistical calculation was

---

772 that we had an all-day flux measurement at each of the two sites. We might be circumspect  
773 about making calculations of the daily divergence when we have such indications of extreme  
774 variability, preferring instead to estimate flux divergence over a somewhat longer time period.

775 The systematic albedo error could be vitiated to some extent if we were to combine the  
776 downwelling shortwave flux with a suitable mean area albedo. At the moment, the MODIS  
777 product appears to represent very well the spatial variability in the albedo, but there are  
778 sufficient differences between it, and the observed albedo at the AMF, and their co-variation  
779 through the year, that require further attention. A possibility for studies at Niamey would be  
780 simply to increase the observed albedo by 0.04, which would correct for most of the  
781 systematic error.

782 Longwave sampling errors appear to be generally smaller than those in the short wave,  
783 although our analysis of this has been somewhat hampered by an apparent calibration  
784 problem. Longwave irradiance is much more uniformly distributed across incoming  
785 directions than shortwave irradiance, and the instantaneous pyrgeometer flux is already a  
786 smooth average. The shortwave irradiance variations are generally dominated by whether or  
787 not there is a direct beam, i.e. whether the sun is obscured by cloud at the measurement site.  
788 Surface temperature variations across our main GERB pixel can be several degrees near  
789 midday, as the MODIS temperature map (Figure 1) shows. However, thanks to the land  
790 surface temperature product generated from SEVIRI, we have seen that there is evidently  
791 some compensation in that areas hotter at midday may be colder at midnight, and so the  
792 average emitted flux, integrated over the day, shows less relative variation than may be  
793 implied by a temperature map generated at a single time of day. The location bias in emitted  
794 longwave flux appears to be no more than about  $4\text{Wm}^{-2}$ , and offsets some of the shortwave  
795 bias arising from the albedo.

796 Measurement of a physical variable only has scientific value when we know the uncertainty  
797 associated with that measurement. Even if the precision and accuracy of such a measurement  
798 should be high, we need to exercise caution if it is being used as an implicit surrogate for  
799 some other quantity. The flux measurements at AMF sites are of the highest quality, give  
800 very accurate values, but have limited spatial support. Treating them, as we do in  
801 RADAGAST, on an equal basis to satellite data that cover much wider areas leaves us with a  
802 tricky sampling issue, only part of which can be tackled by characterising, and compensating  
803 for, the heterogeneities of the land surface within that area that affect our estimate of

---

804 upwelling fluxes. In our particular case a second set of ground flux measurements was found  
805 to be invaluable in helping to understand and bound the likely estimation error for the  
806 downwelling fluxes. It is unlikely that the presence of a third or fourth station would help  
807 much more, beyond enabling us to test some of the assumptions about stationarity that were  
808 used in deriving the lower bound of our sampling error variance of the irradiance fields. Most  
809 of the benefit comes from just the first additional station, and the relatively small additional  
810 cost of a secondary site during such an ambitious project seems a small price to pay for the  
811 ability to place an error bar on our flux calculations. Thanks are due to the ARM team for  
812 their far-sightedness in including this additional resource in the RADAGAST project.

## 813 **7 ACKNOWLEDGMENTS**

814 Several rounds of thanks are owed to the Atmospheric Radiation Measurement program.  
815 First, for providing the Mobile Facility and managing to keep it running almost continuously  
816 for over twelve months, often in difficult conditions. Further, the rapid availability of the  
817 data, and the deceptive simplicity of its distribution through a most excellent web interface.  
818 Discussions with Mark Miller and Chuck Long were of enormous benefit in understanding  
819 instrumental errors. Ben Johnson and Jim Hayward of the UK Met Office kindly made  
820 available to us the albedo data used for Figure 14, acquired during the DABEX campaign.  
821 Special thanks to Chrystal Schaffe and the MODIS team at the university of Boston for  
822 generating the version 5 albedo data for Niamey ahead of its scheduled upgrade.

---

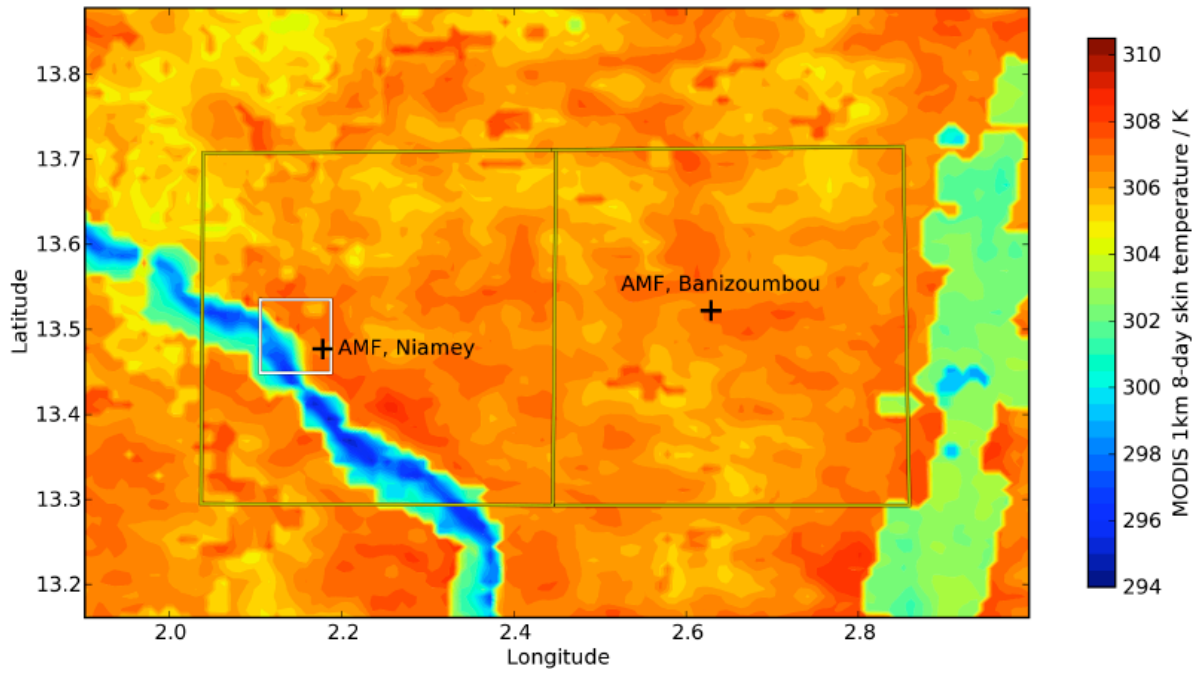
823

## 8 REFERENCES

- 824 Becker, F., and Z. L. Li (1990). Toward a local split window method over land surface. *Int. J.*  
825 *Remote Sens.* 11, 369-393.
- 826 Bharmal, N. A., A. Slingo, G. J. Robinson and J. J. Settle, 2008. Simulation of surface and top  
827 of atmosphere thermal fluxes and radiances from the RADAGAST experiment. *J. Geophys.*  
828 *Res.*, submitted
- 829 DeWitt, S., L. Gonzalez, N. Clerbaux, A. Ipe, C. Bertrand, and B. De Paepe 2008 *The*  
830 *Geostationary Earth Radiation Budget Edition 1 data processing algorithms* Advances in  
831 Space Science Vol 41 pp 1906-1913.
- 832 Dutton, E. G., P Gotseff and C.N. Long 2008 Investigation of the downwelling LW  
833 differences between the Niamey AMF Main and supplementary sites DOE/SC-ARM/TR-083
- 834 Harries, J.E. and 42 others, 2005. *The Geostationary Earth Radiation Budget (GERB) project.*  
835 *Bull. Am. Meteorol. Soc.*, Vol 86 pp945-960
- 836 Haywood, J. M, et al., 2008. Overview of the Dust and Biomass burning Experiment and  
837 African Monsoon Multidisciplinary Analysis Special Observing Period-0. *J. Geophys. Res.*,  
838 submitted for publication in DABEX special section
- 839 Kiehl, J. T. and K. E. Trenberth, 1997. Earth's Annual Global Mean Energy Budget *Bull.*  
840 *Amer. Meteor. Soc.* 78, 197-208
- 841 Miller , M. A and A. Slingo, 2007 *The ARM Mobile Facility and its first international*  
842 *deployment: measuring radiative flux divergence in West Africa* *Bull. Am. Meteorol. Soc.*,  
843 Vol. 88, pp1229-1224
- 844 Price, J. C. (1984), Land surface temperature measurements from the split window channels  
845 of the NOAA-7/AVHRR. *J. Geophys. Res.* 89: 7231-7237.
- 846 Redelsperger, J.-L., C. D. Thorncroft, A. Diedhiou, T. Lebel, D. J. Parker and J. Polcher,  
847 2006. African Monsoon Multidisciplinary Analysis. An international research project and  
848 field campaign. *Bull. Am. Meteorol. Soc.*, **87**, 1739-1746
- 849 Schaaf, C. and 21 others (2002) First operational BRDF, albedo nadir reflectance from  
850 MODIS, *Remote Sensing of Environment*, Vol 83 pp 135-148
- 851 Schmetz, J.P., P. Pili, S. Tjemkes, D. Just, J. Kerkmann, S. Rota and A. Ratier (2002) An  
852 introduction to Meteosat Second Generation (MSG) *Bull. Am. Meteorol. Soc.*, Vol 83 pp977-  
853 992
- 854 Seemann, S.W., E. E. Borbas, R. O. Knuteson, G. R. Stephenson, H.-L. Huang, 2007:  
855 *Development of a Global Infrared Land Surface Emissivity Database for Application to Clear*  
856 *Sky Sounding Retrievals from Multi-spectral Satellite Radiance Measurements.* *J. of Appl.*  
857 *Meteor. and Climatol.*, Vol. 47, 108-123.
- 858 Settle, J.J. (2004). *On the use of remotely sensed data for the estimation of spatially averaged*  
859 *geophysical variables* *IEEE Trans. Geoscience and Remote Sensing* Vol 42 pp. 620-631

- 
- 860 Slingo, A., et al., 2006. Observations of the impact of a major Saharan dust storm on the  
861 atmospheric radiation balance. *Geophys. Res. Lett.*, **33** (24), L24817, doi:  
862 10.1029/2006GL027869
- 863 Slingo, A, H.E. White, N.A. Bharmal and G.J. Robinson, (2008) Overview of observations  
864 from the RADAGAST experiment in Niamey, Niger. Part 2: Radiative fluxes and divergences  
865 *Journal of Geophysical Research*, submitted.
- 866 Sobrino, J.A. and M. Romaguera (2004) Land Surface temperature retrieval from MSG1-  
867 SEVIRI data *Remote Sensing of Environment* Vol. 92 pp 247-254
- 868 Wild, M., A. Ohmura, H. Gilgen & E. Roeckner (1995) *Validation of general Circulation*  
869 *Model radiative Fluxes Using Surface Observations* *Journal of Climate*, Vol. 8, 1309-1324

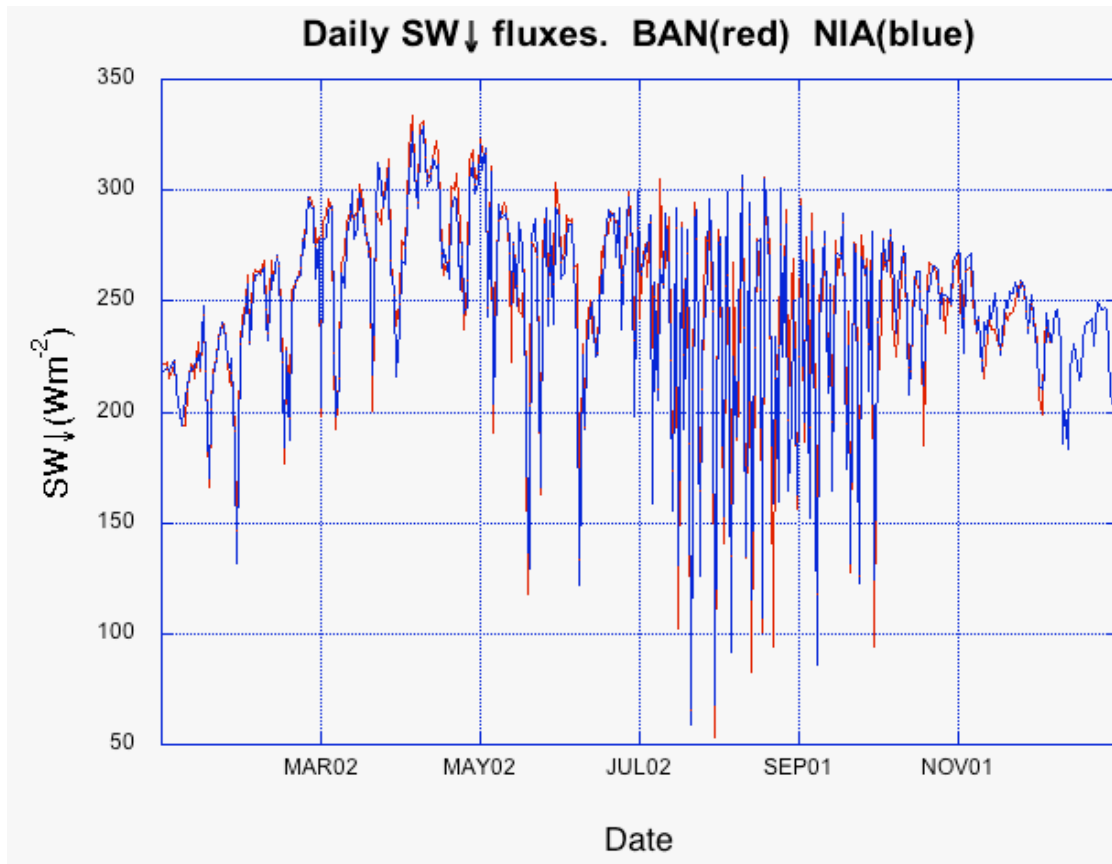
870



871

872 **Figure 1** Locations of the two AMF deployments, and the outlines of two adjacent  
873 **GERB** pixels.

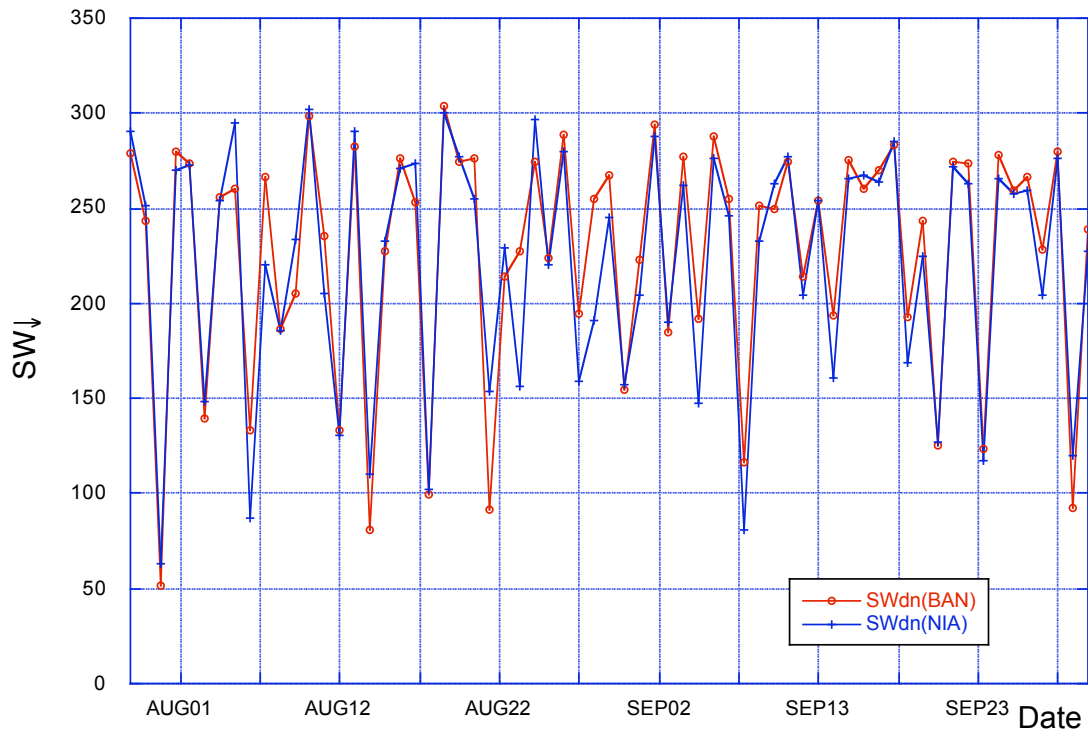
874



875

876 **Figure 2 Short wave downwelling fluxes (daily averages) in 2006**

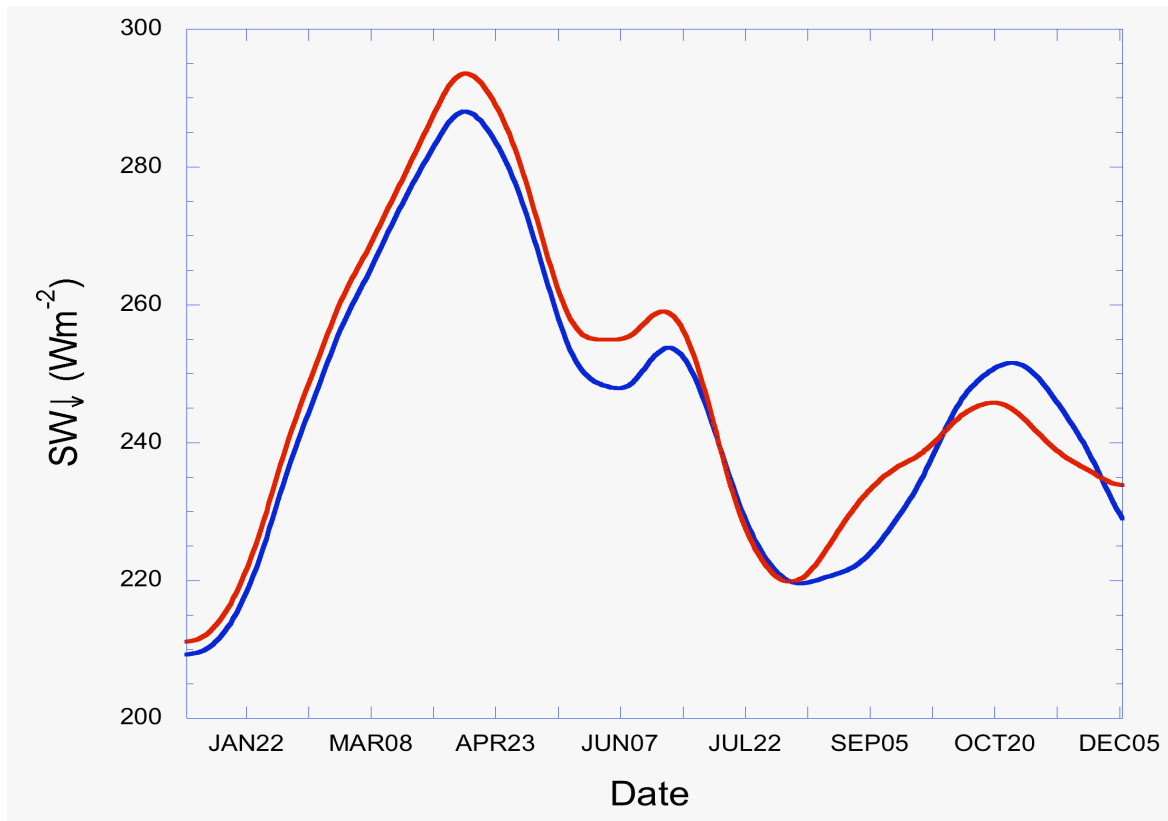
877



878

879 **Figure 3 SW fluxes (daily averages,  $Wm^{-2}$ ) in August and September**

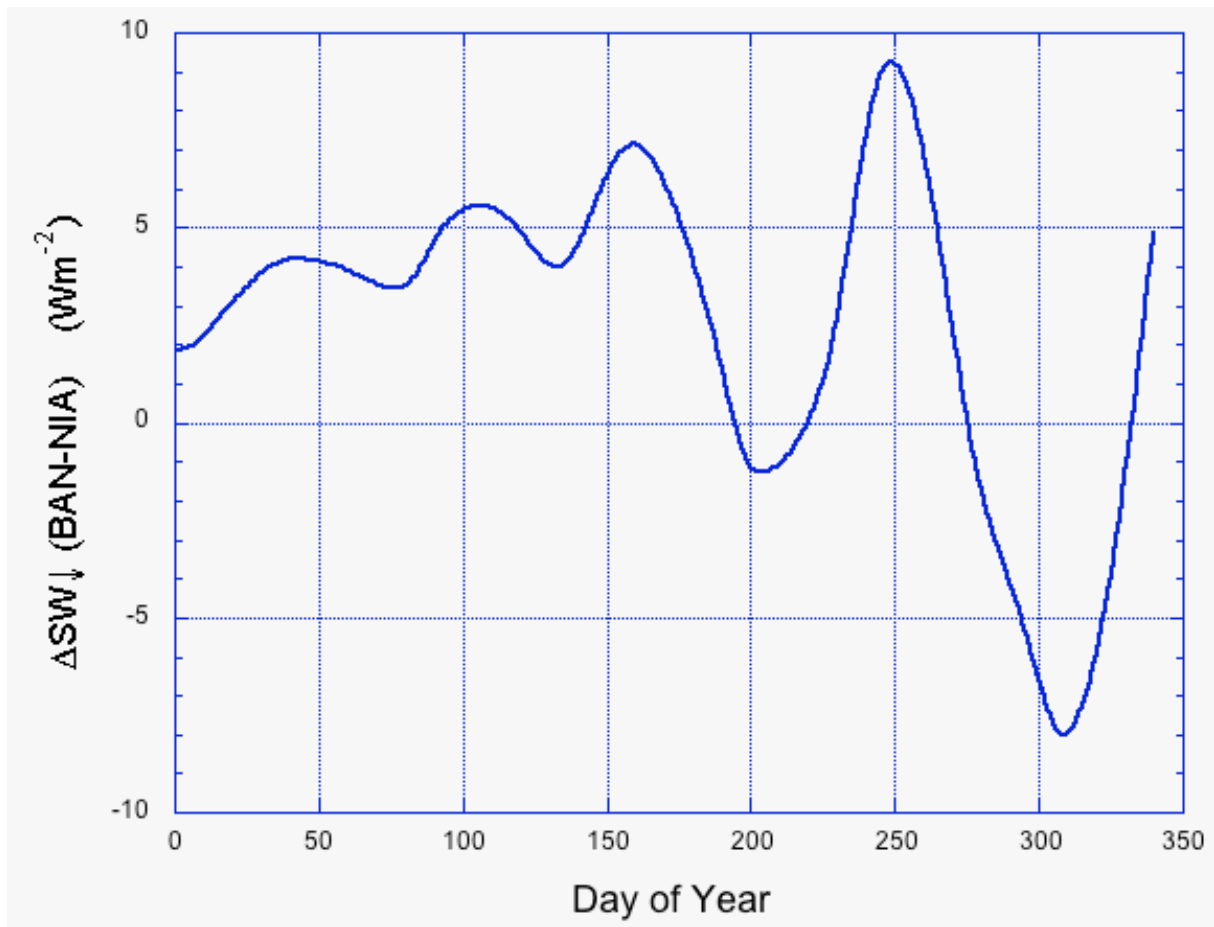
880



881

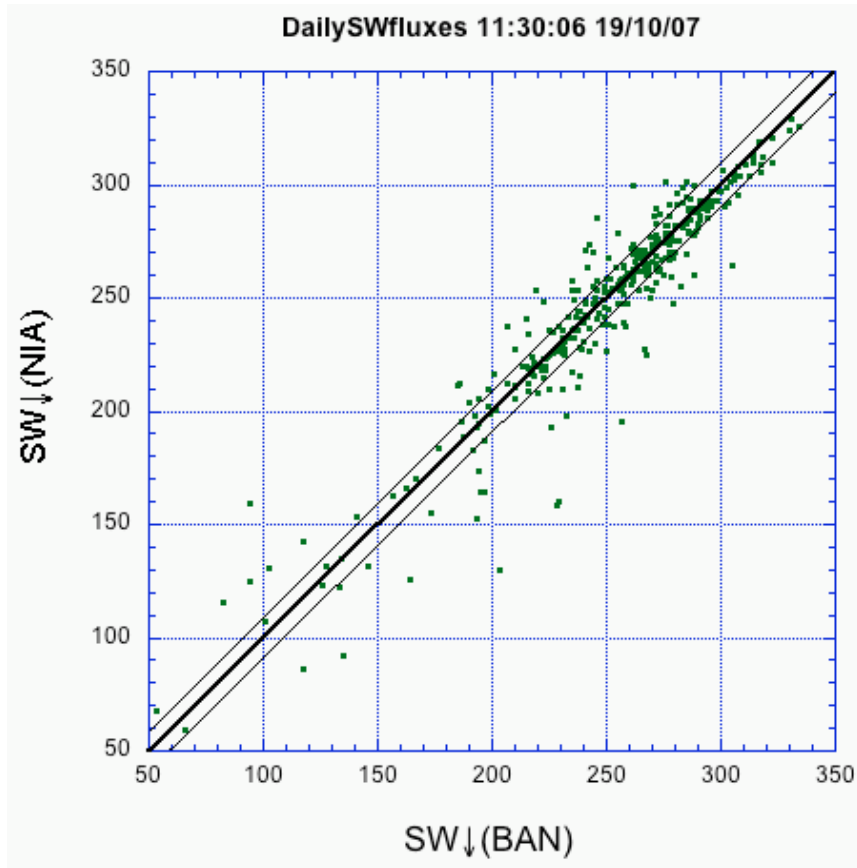
882 **Figure 4 Shortwave Irradiance, smoothed. Red =BAN, Blue = NIA**

883



884

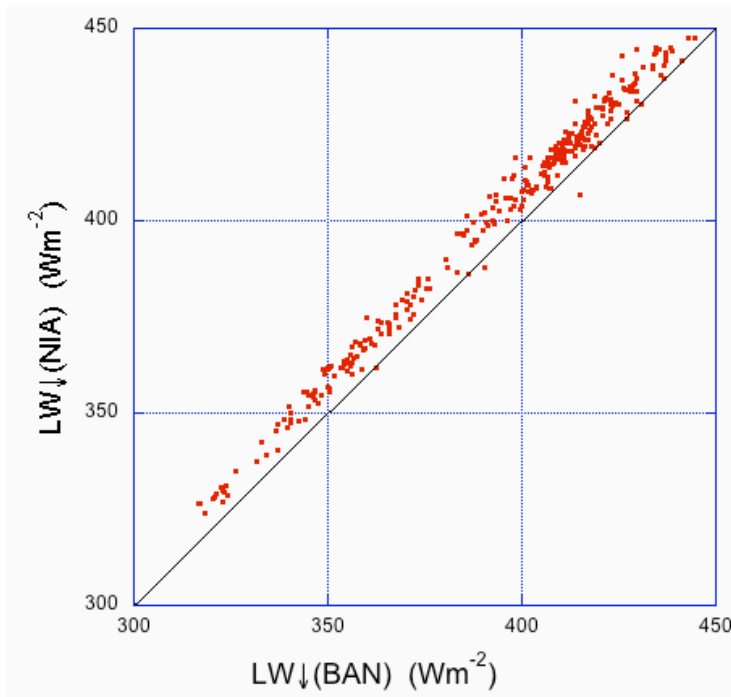
885 **Figure 5 SW Irradiance difference, BAN-NIA, (smoothed).**



886

887 **Figure 6 Scatterplot of SW Irradiances. The heavy line is the 1-1 line, and the parallel**  
888 **lines are displaced by 10Wm<sup>-2</sup>.**

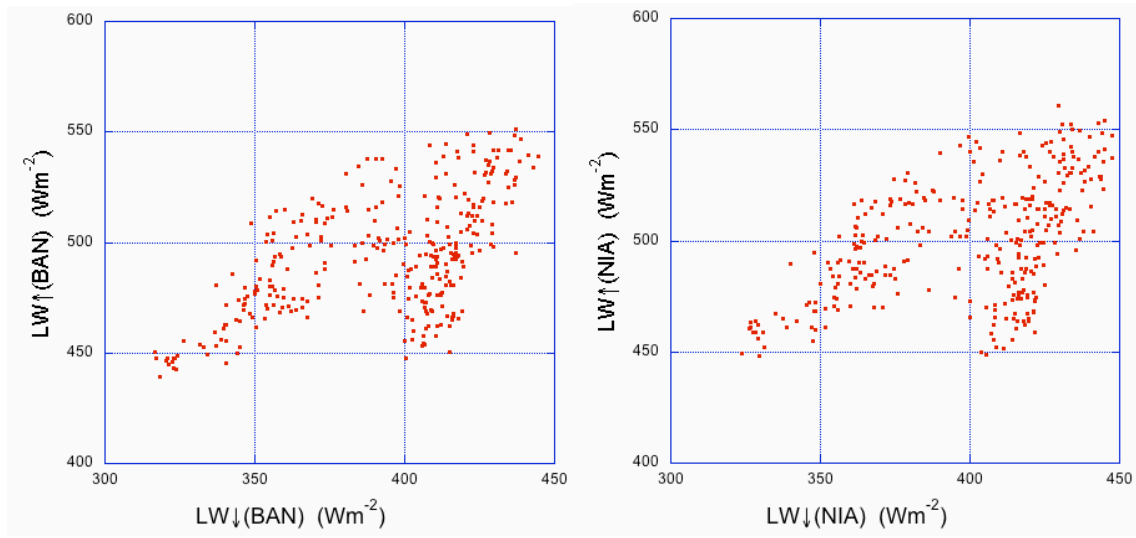
889



890

891 **Figure 7 LW downward fluxes. The correlation coefficient is 0.995.**

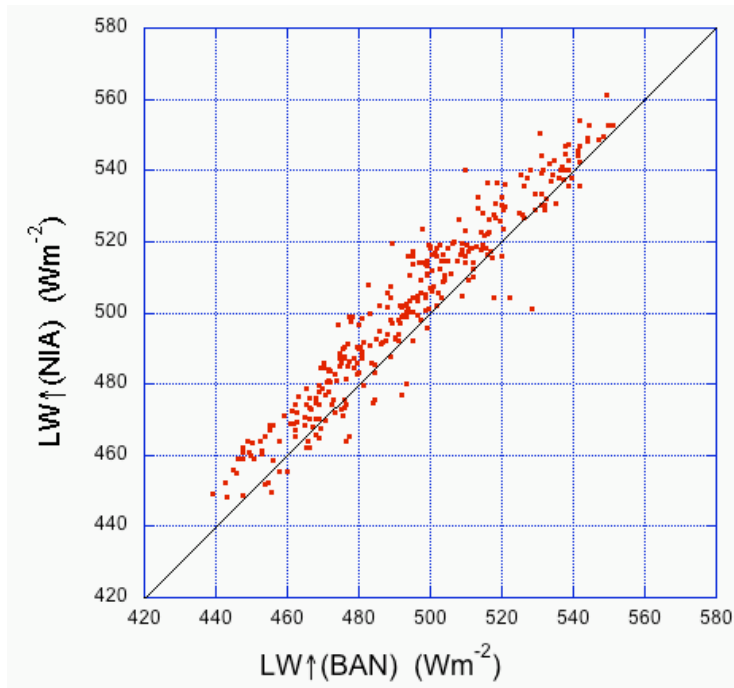
892



893

894 **Figure 8 Upward and downward LW fluxes**

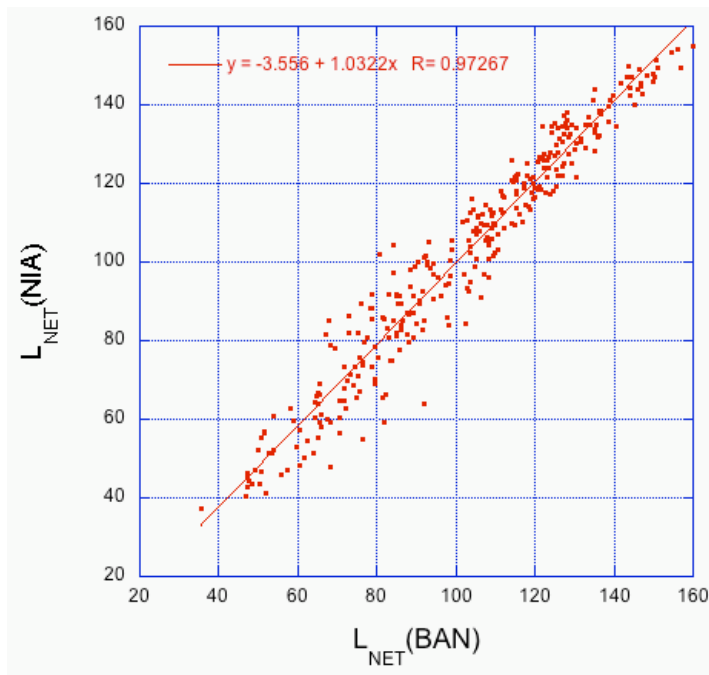
895



896

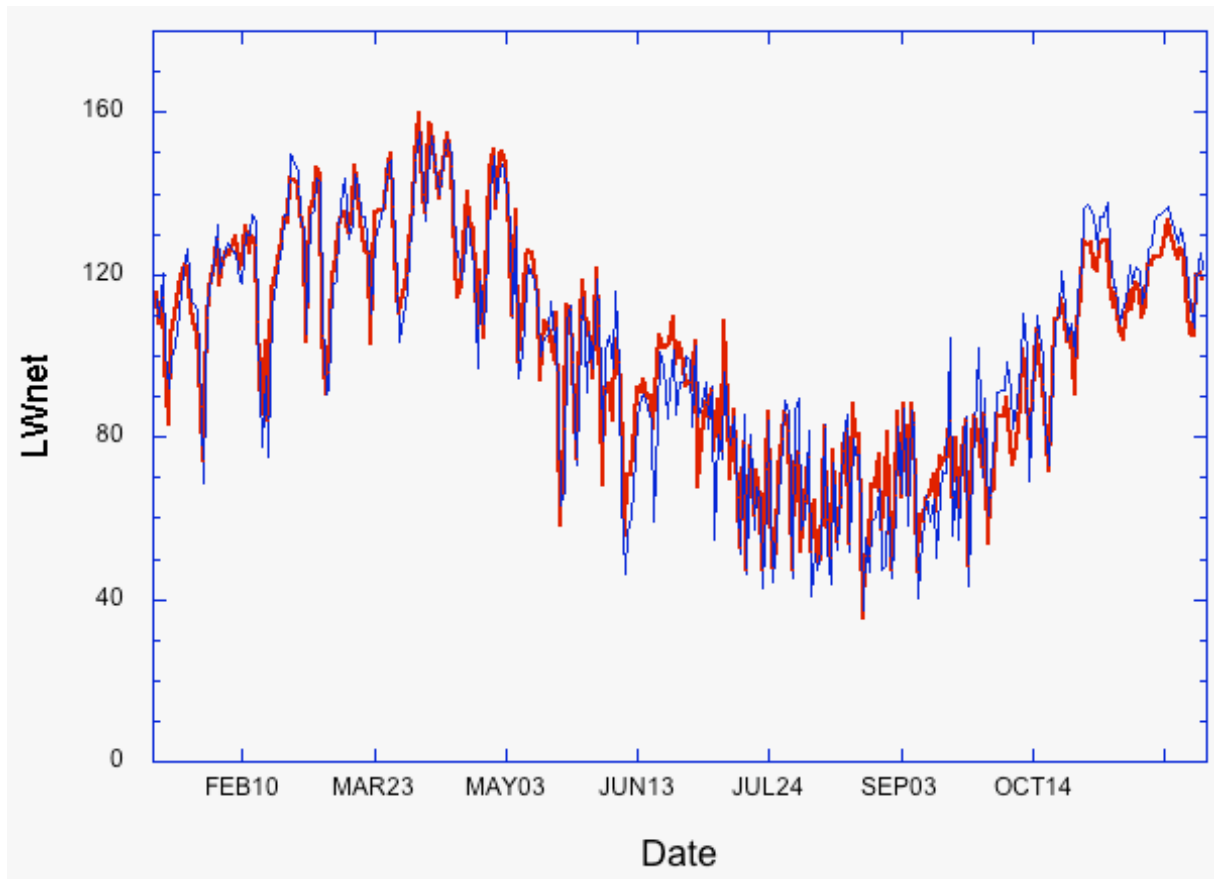
897 **Figure 9 Comparison of upwelling LW flux. Correlation = 0.96**

898



899

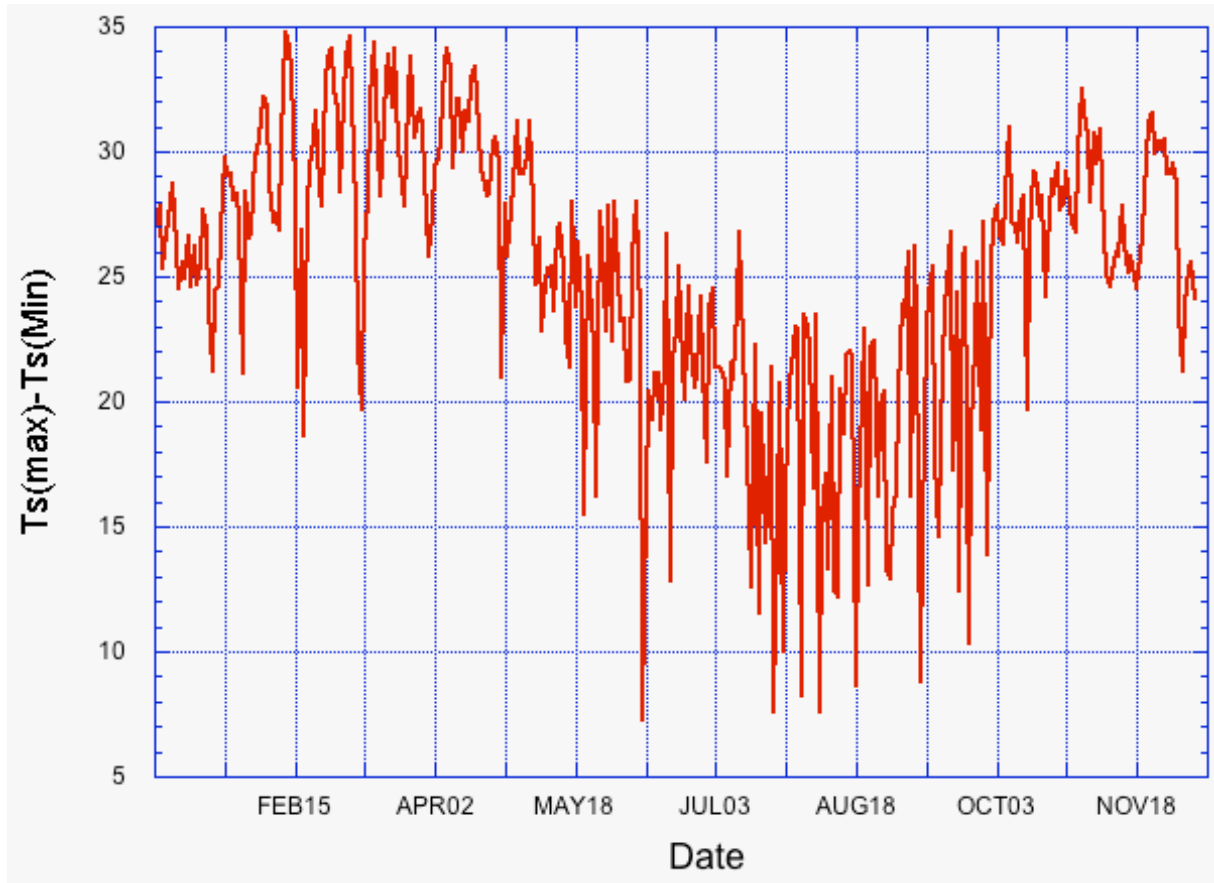
900 **Figure 10** Scatterplot of net LW fluxes at the two sites



901

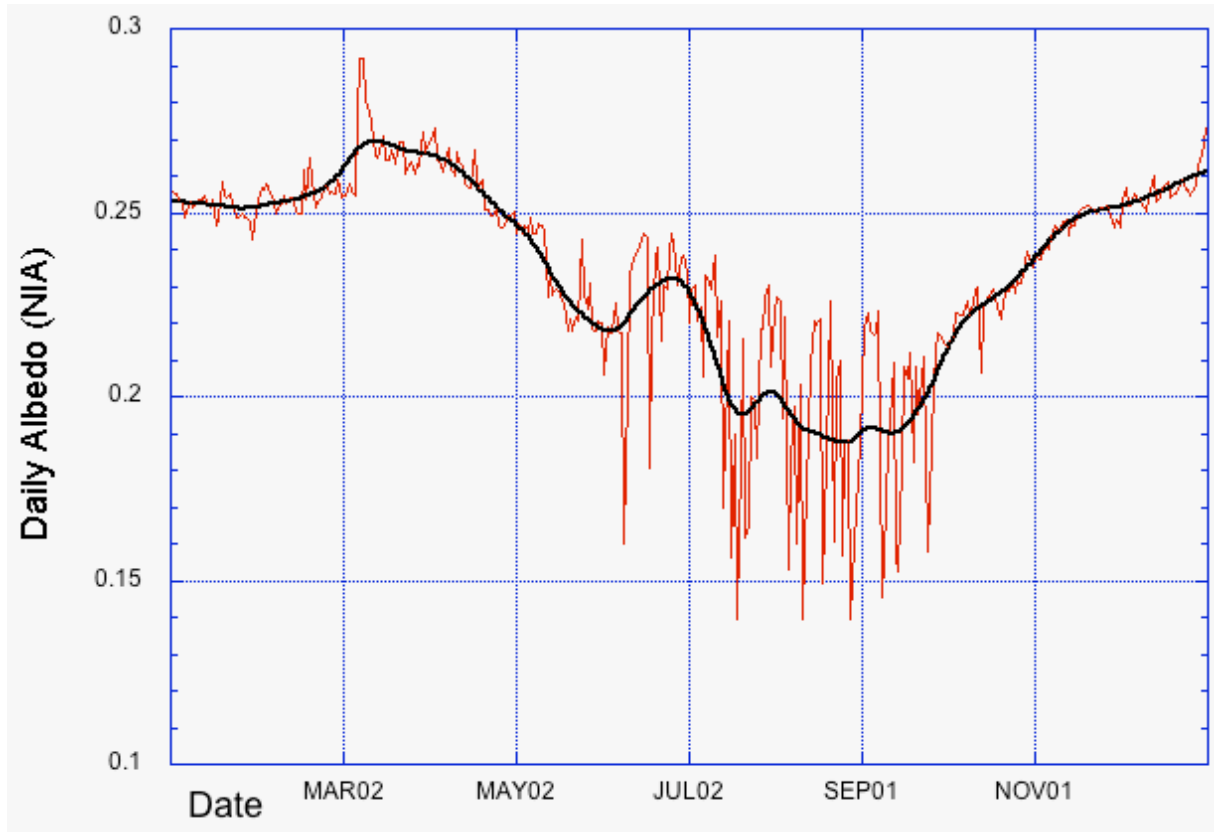
902 **Figure 11 Net Longwave Fluxes ( $\text{Wm}^{-2}$ ) Red=BAN, Blue=NIA**

903



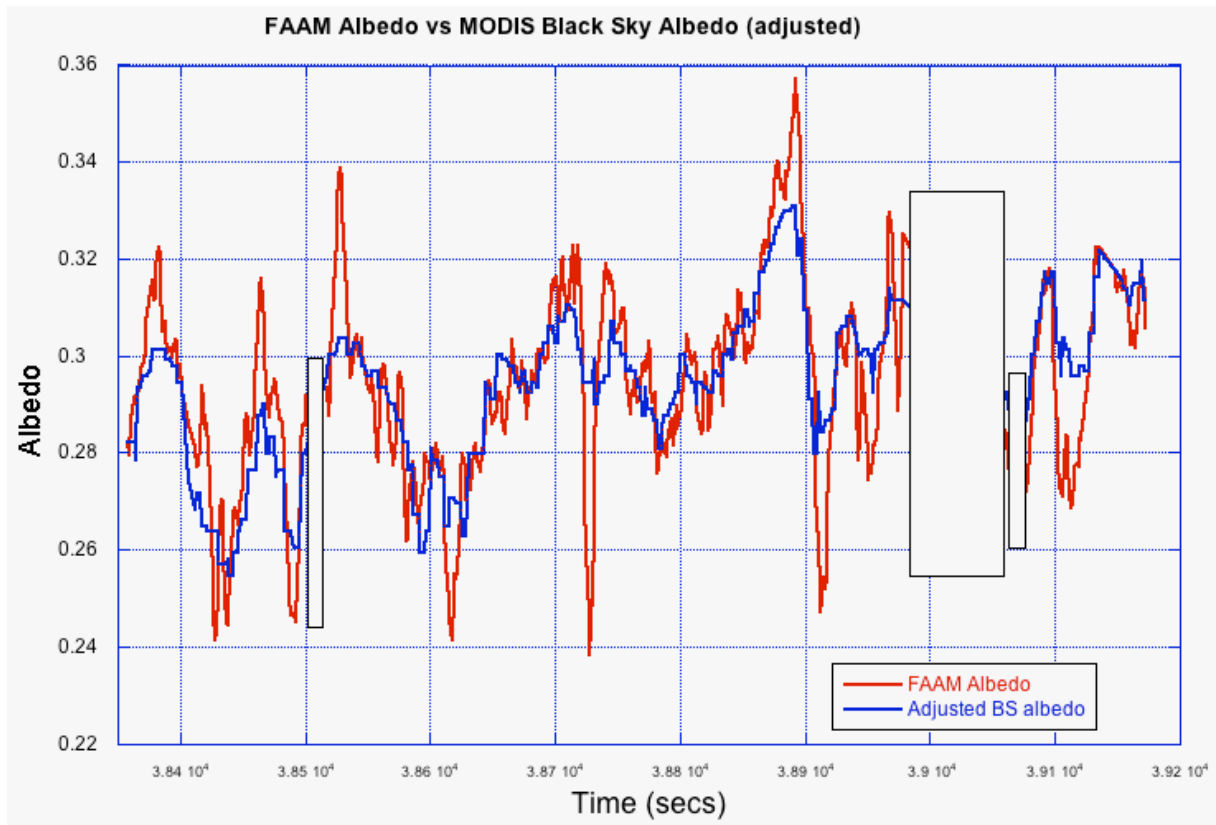
904

905 **Figure 12 IRT Surface temperature range at NIA (K)**



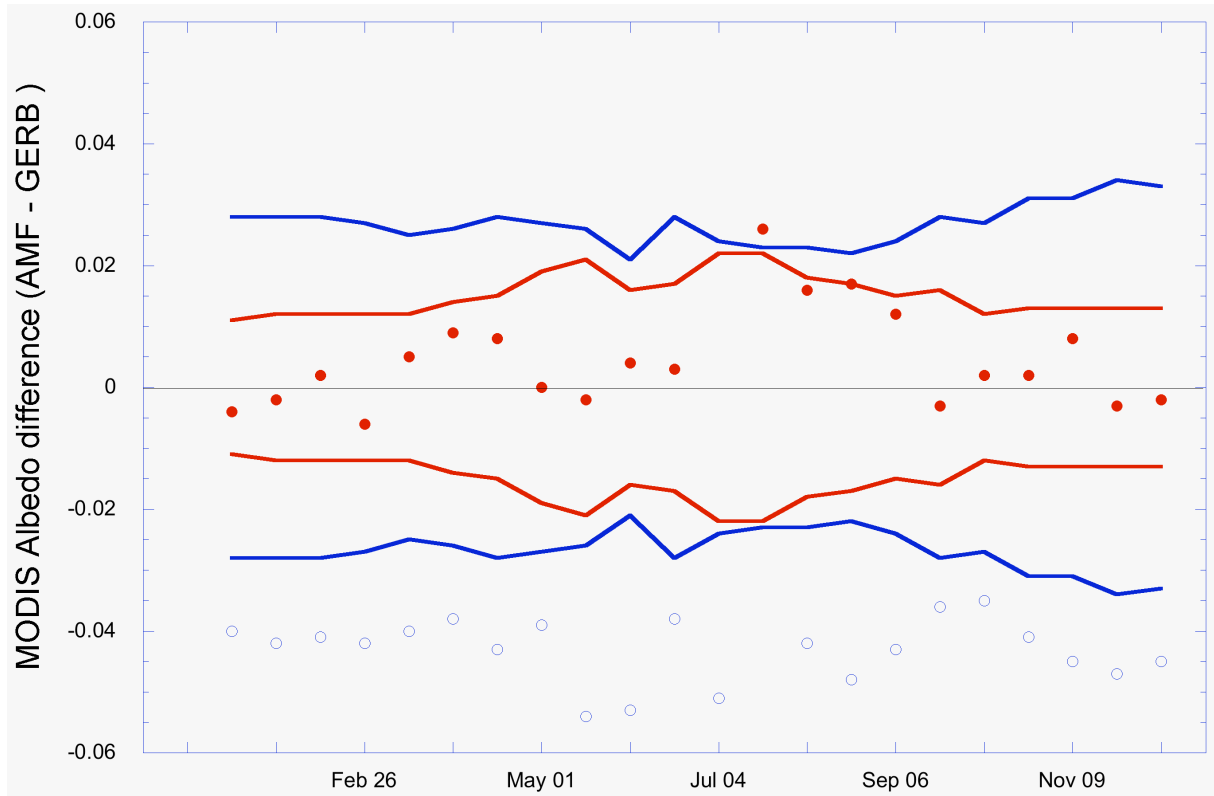
906

907 **Figure 13 Variations of the daily Albedo at NIA**



908

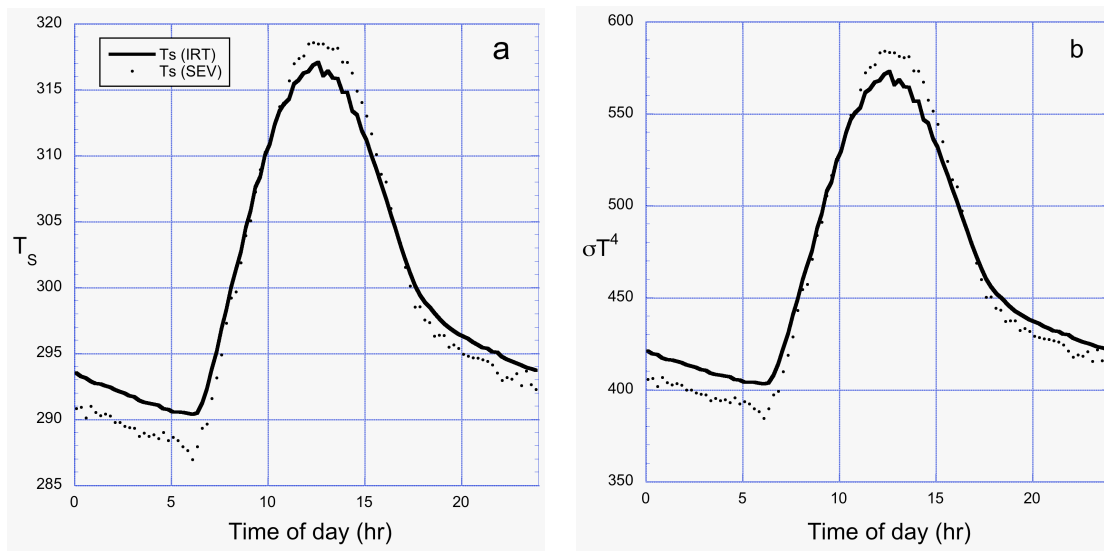
909 Figure 14 Albedo comparison, FAAM and MODIS V5. NIA is at the beginning of the flight  
 910 (left of plot) BAN at the end,



911

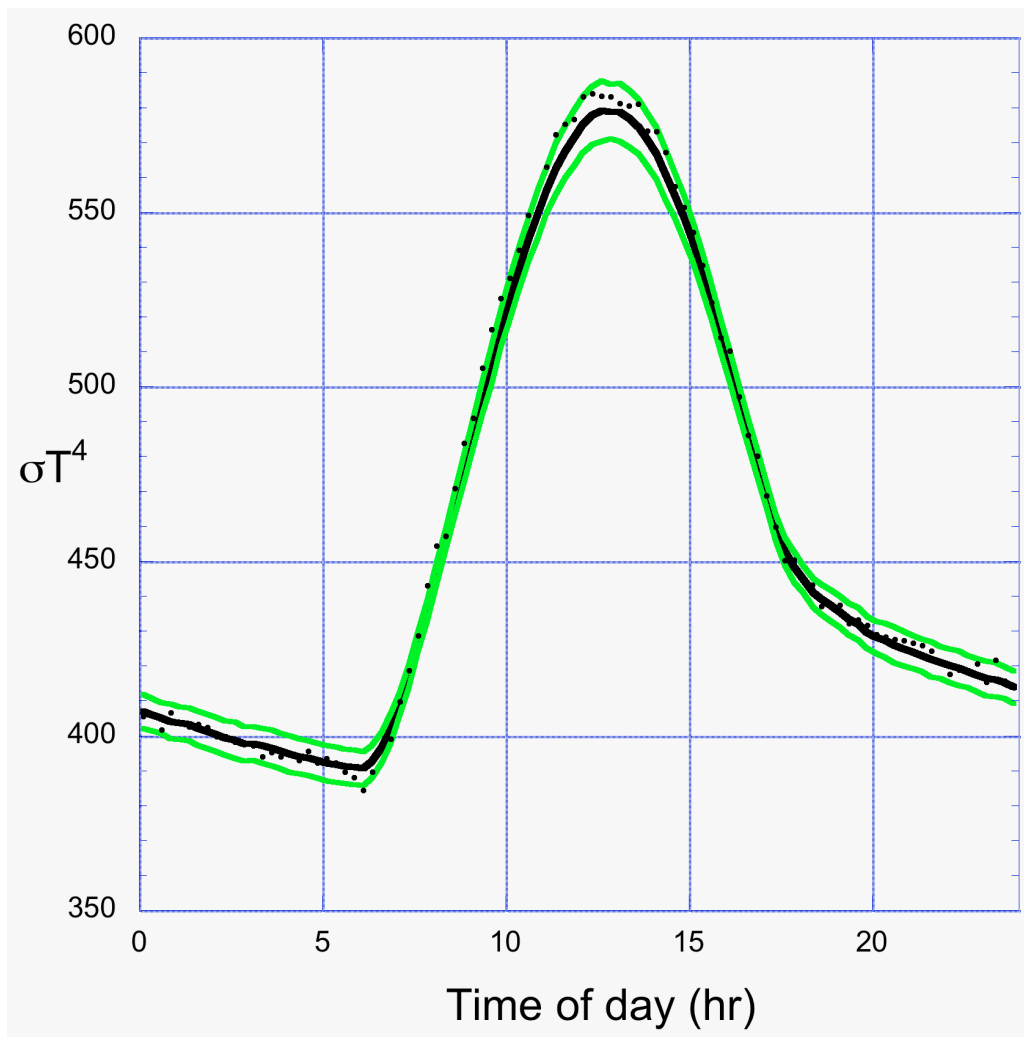
912 **Figure 15 Albedo "errors" from MODIS 500m albedo retrievals. Circles represent the**  
 913 **differences (AMF value minus area mean); curves show  $\pm 1$  standard deviation of the**  
 914 **MODIS values within a GERB pixel. Red = BAN, Blue = NIA**

915



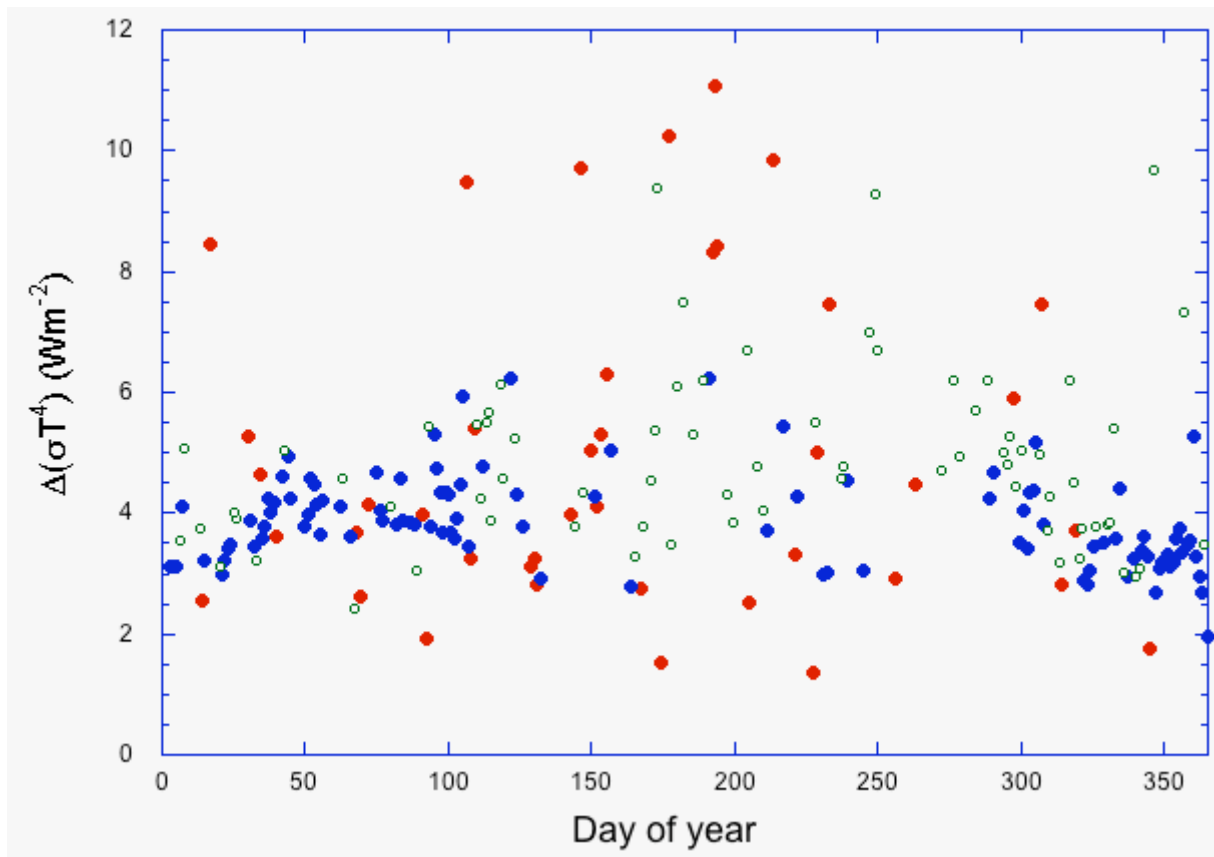
916

917 Figure 16 Surface temperature (left) and black body flux from the Infrared Thermometer at  
918 the AMF (solid line) and from SEVIRI retrieval (dots)



919

920 **Figure 17 Mean and mean  $\pm$  1sd curves of SEVIRI-derived  $\sigma T^4$  (see text for detail).**



921  
922 **Figure 18** Variability of  $\sigma T^4$  around NIA, variation in time. Blue circles represents  
923 values in which the confidence index is  $>0.8$ , red circles those for which the confidence is  
924  $<0.2$

925

---

	NIA	BAN	BAN-NIA
Mean	245.29	248.52	3.23
Median	256.00	256.95	2.76
St. Dev	45.78	45.19	14.89
Range	57:325	52:332	-64:75

927 **Table 1 SW Irradiance statistics for 2006 (331 days) (units are  $\text{Wm}^{-2}$ ).**

928

	Downwelling (Wm <sup>-2</sup> )			Upwelling (Wm <sup>-2</sup> )			Net (Wm <sup>-2</sup> )		
	NIA	BAN	B-N	NIA	BAN	B-N	NIA	BAN	B-N
Mean	399.27	391.77	-7.49	500.54	493.32	-7.22	101.55	101.27	-0.28
Median	410.09	402.71	-7.60	500.95	493.36	-7.68	105.07	105.33	-0.63
s.d	31.79	32.09	3.27	26.64	26.54	7.59	27.52	29.20	7.01
Range	324:448	317:445	-18:8	448:558	439:551	-43:28	35:160	37:155	-28:34

929 Table 2 LW statistics for 2006 (323 days).

	Longwave					Shortwave				
	Nd	NIA		BAN		Nd	NIA		BAN	
		Mean	sd	Mean	sd		Mean	sd	Mean	sd
J	17	368.04	19.64	360.50	19.77	29	211.22	22.14	213.01	20.78
F	28	365.70	21.23	356.63	20.31	28	250.94	26.94	255.25	26.75
M	29	379.31	14.92	372.28	15.31	29	264.44	31.74	269.12	33.75
A	30	433.83	21.76	386.23	22.18	29	286.30	25.89	292.88	26.19
M	30	431.93	12.87	423.32	15.21	30	259.66	48.30	262.83	45.95
J	30	432.65	11.14	425.42	10.52	30	251.68	37.82	259.27	34.48
J	30	422.61	8.33	415.71	7.57	29	233.57	65.79	237.93	61.66
A	31	416.34	7.04	410.10	7.03	31	221.78	64.70	224.51	65.52
S	30	414.40	6.78	407.89	6.47	30	226.51	58.93	234.05	56.48
O	31	411.54	16.97	402.04	17.76	31	252.05	18.53	249.57	20.60
ND	35	348.20	17.58	344.16	17.63	35	241.73	16.52	239.67	15.25
All	321	399.33	31.66	391.84	32.03	331	245.29	45.78	248.52	45.19

931 **Table 3 Statistics of the Monthly Downwelling Fluxes (flux units are  $Wm^{-2}$ )**

---

932

	JAN	FEB	MAR	APR	MAY	JUN	JUL	AUG	SEP	OCT	NOV	DEC
$\mu$	0.252	0.255	0.267	0.258	0.233	0.225	0.209	0.189	0.198	0.226	0.247	0.256
sd	0.003	0.004	0.008	0.003	0.006	0.017	0.022	0.027	0.023	0.005	0.002	0.004
PPT	0.123	0	0	0	0.334	1.446	13.65	11.00	3.780	0.331	0.021	0

933

**Table 4 NIA albedo, monthly mean and standard deviation, and rainfall**

---

934

	JAN	FEB	MAR	APR	MAY	JUN	JUL	AUG	SEP	OCT	NOV	DEC
$\mu$	0.313	0.309	0.318	0.318	0.304	0.291	0.265	0.238	0.225	0.241	0.280	-
sd	0.003	0.004	0.011	0.006	0.007	0.011	0.016	0.013	0.009	0.004	0.004	-
PPT	0.001	0.001	0.002	0.001	0.381	3.342	19.65	17.91	7.142	0.026	0.010	-

935

**Table 5 BAN albedo, monthly mean and standard deviation, and rainfall**

Start_Day	NIA				BAN			
	$a_A$	sd	$a_N$	$a_A - a_N$	$a_A$	sd	$a_B$	$a_A - a_N$
Jan 09	.245	.028	0.205	.040	.266	.011	.262	.004
Jan 25	.252	.028	0.210	.042	.280	.012	.278	.002
Feb 10	.263	.028	0.222	.041	.292	.012	.294	-.002
Feb 26	.274	.027	0.232	.042	.299	.012	.293	.006
Mar 14	.281	.025	0.241	.040	.308	.012	.313	-.005
Mar 30	.282	.026	0.244	.038	.309	.014	.318	-.009
Apr 15	.274	.028	0.231	.043	.301	.015	.309	-.008
May 01	.267	.027	0.228	.039	.298	.019	.298	0
May 17	.257	.026	0.203	.054	.283	.021	.281	.002
Jun 02	.270	.021	0.217	.053	.292	.016	.296	-.004
Jun 18	.277	.028	0.239	.038	.313	.017	.316	-.003
Jul 04	.257	.024	0.206	.049	.289	.022		-
Jul 20	.246	.023		-	.274	.022	.300	-.026
Aug 05	.235	.023	0.193	.042	.255	.018	.271	-.016
Aug 21	.241	.022	0.193	.048	.260	.017	.277	-.017
Sep 06	.229	.024	0.186	.043	.251	.015	.263	-.012
Sep 22	.234	.028	0.198	.036	.260	.016	.257	.003
Oct 08	.240	.027	0.205	.035	.265	.012	.267	-.002
Oct 24	.249	.031	0.208	.041	.273	.013	.275	-.002
Nov 09	.261	.031	0.216	.045	.287	.013	.295	-.008
Nov 25	.264	.034	0.217	.047	.290	.013	.287	.003
Dec 11	.268	.033	0.223	.045	.295	.013	.293	.002

937 Table 6 MODIS albedos: AMF pixel and GERB area averages On two occasion(blank  
938 entries) MODIS was unable to retrieve a value for the pixel containing the AMF.

---

939

	J	F	M	A	M	J	J	A	S	O	ND	All
$\rho$	0.83	0.77	1.15	1.40	1.32	1.24	0.81	0.75	1.37	0.86	0.66	1.20
Diff	1.87	2.01	2.50	3.45	2.89	2.52	1.73	1.21	2.79	2.33	1.42	2.33

940 **Table 7 Limits of LW irradiance sampling error, by month**

---

941

	$\epsilon_{\min}$	$\epsilon_{\text{mean}}$	$\sqrt{V(\epsilon)}$	$\epsilon_{\max}$
JAN	0.928	0.936	0.003	0.946
SEP	0.919	0.935	0.004	0.944

942 **Table 8 Variability of Emissivity in the NIA GERB pixel**

943

	Albedo		U <sub>1</sub>		U <sub>2</sub>		U <sub>3</sub>		U <sub>1</sub> +U <sub>3</sub>		U <sub>4</sub>		U	
	NIA	BAN	NIA	BAN	NIA	BAN	NIA	BAN	NIA	BAN	NIA	BAN	NIA	BAN
Jan	0.252	0.313	±2.75	±2.52	8.45	-2.14	±1.70	±1.70	±2.26	±2.20	-4	0	4.45±2.26	-2.14±2.20
Feb	0.255	0.309	±2.35	±2.49	10.04	-2.56	±1.86	±1.86	±2.21	±2.07	-4	0	6.04±2.21	-2.56±2.07
Mar	0.266	0.317	±3.01	±2.80	10.58	-2.71	±2.30	±2.30	±3.20	±3.00	-4	0	6.58±3.20	-2.71±3.00
Apr	0.259	0.318	±3.85	±3.54	11.45	-2.92	±2.85	±2.85	±3.40	±3.15	-4	0	7.45±3.40	-2.92±3.15
May	0.234	0.304	±7.80	±7.52	10.39	-2.62	±2.66	±2.66	±7.89	±7.20	-4	0	6.39±7.89	-2.62±7.20
Jun	0.226	0.293	±5.60	±5.12	10.07	-2.60	±2.32	±2.32	±6.03	±5.57	-4	0	6.07±6.03	-2.60±5.57
Jul	0.222	0.269	±9.12	±8.57	9.34	-2.38	±1.64	±1.64	±9.34	±8.79	-4	0	5.34±9.34	-2.38±8.79
Aug	0.196	0.240	±12.00	±11.35	8.87	-2.24	±1.63	±1.63	±12.2	±11.55	-4	0	4.87±12.2	-2.24±11.6
Sep	0.200	0.225	±6.89	±6.67	9.06	-2.30	±2.65	±2.65	±7.00	±6.79	-4	0	5.06±7.00	-2.30±6.79
Oct	0.226	0.240	±4.77	±4.68	10.08	-2.47	±2.15	±2.15	±4.66	±4.54	-4	0	6.08±4.66	-2.47±4.54
Nov/D	0.248	0.282	±3.25	±3.10	9.67	-2.40	±1.29	±1.29	±3.10	±2.96	-4	0	5.67±3.10	-2.40±2.96

**Table 9 Contributions to the sampling error. Apart from albedos, all entries have units of  $Wm^{-2}$ .**